University of Rhode Island

DigitalCommons@URI

Open Access Master's Theses

2017

Mineral Identification and Preliminary Mapping of Organic Compounds in Serpentinite-Related Lithologies Using **μ**FTIR

Abigail M. Johnson
University of Rhode Island, abigail_johnson@uri.edu

Follow this and additional works at: https://digitalcommons.uri.edu/theses

Terms of Use
All rights reserved under copyright.

Recommended Citation

MINERAL IDENTIFICATION AND PRELIMINARY

MAPPING OF ORGANIC COMPOUNDS IN

SERPENTINITE-RELATED LITHOLOGIES USING μFTIR

BY

ABIGAIL M. JOHNSON

A THESIS SUBMITTED IN PARTIAL FULFILLMENT OF THE

REQUIREMENTS FOR THE DEGREE OF

MASTER OF SCIENCE

IN

ENVIRONMENTAL AND EARTH SCIENCES

UNIVERSITY OF RHODE ISLAND

2017

MASTER OF SCIENCE THESIS

OF

ABIGAIL M. JOHNSON

APPROVED:

    Thesis Committee:

    Major Professor   Dawn Cardace

                              Bethany Jenkins

                              David Smith

                              Nasser H. Zawia
                    DEAN OF THE GRADUATE SCHOOL

UNIVERSITY OF RHODE ISLAND
2017

ABSTRACT

Serpentinization, the water-rock reaction forming serpentine mineral assemblages from olivine and pyroxene-bearing protoliths, can co-occur with the production of hydrogen, methane, and diverse organic compounds. Serpentinization is regarded as a geologic process important to the sustainability of the deep biosphere and the origin of life. Serpentinization has been found to support metabolisms involving anaerobic CO-oxidation, acetogenesis, reduction of sulfur compounds, H_2 oxidation, CO_2 fixation, magnetite reduction, and fermentation. There is on-going research to develop a method that can visually depict mineral associations in serpentinites with serpentinization-related organics. In this report, we describe new findings, using μFTIR to map minerals and associated organics related to serpentinization. To do this, we identified, confirmed, and documented FTIR wavenumber regions linked to (I) serpentinization-associated minerals and embedded organics, (II) carbonate-associated minerals, and (III) a polysaccharide proxy for EPS. The findings of this study indicate that organic presence with a mineral background can be detected using reflection mode-μFTIR (R-FTIR) and transmission mode-μFTIR (T-FTIR). Implications of this study include increased prospects for use of FTIR in interrogating polished rock surfaces to determine the association of organics to mineral phases and boundaries in serpentinization-related lithologies.

ACKNOWLEDGMENTS

Many thanks go to my major committee advisor, Dawn Cardace, for her never-ending support and encouragement over the years. I am honored to have had the opportunity to spend time in Dawn's lab learning from her and developing the invaluable laboratory and analytical skills I have gained on this journey. I also thank my other committee members, Bethany Jenkins and David Smith, for their support and guidance.

Thank you also to all who helped in the lab: Alexander Sousa for helping with μFTIR troubleshooting, Roger Hart, Paige McLaughlin, and Chelsea Errichetti for running XRD on sample set, and Caroline Amelse for helping polish samples.

I would also like to thank my family and friends, because without their support, love, and encouragement, I would not have pursued what seemed to be a daunting and challenging career path.

PREFACE

This thesis is in manuscript format and has been prepared for publication in the journal *American Mineralogist*, but has not yet been submitted, and all formatting has been adapted to the specifications of that journal. Certain undeclared chapters and sections will be used in publication, however at the time of the completion of this thesis, those specific parts are unknown.

TABLE OF CONTENTS

LIST OF TABLES

LIST OF FIGURES

INTRODUCTION

Until recently, society believed the ocean floor to be flat, with little/no life at the water-sediment interface, and with a barren subsurface (Jorgensen 2012). With ever-increasing interest in finding the limits of life on Earth, we have since discovered the immense deep biosphere adapted to extreme temperatures, pressures, pH and nutrient conditions (Jorgensen 2012; Colwell and D'Hondt 2013; Orcutt et al. 2013). Although energy levels are about 10,000 times lower than surface ecosystems (Parkes et al. 2014), and about ~48% of the ocean floor is made up of low productivity sites, such as the subtropical gyres (D'Hondt et al. 2009), there still exists in the global sub-seafloor an estimated cell count between 2.9×10^{29} (Jorgensen 2012) and 5.39×10^{29} (Parkes et al. 2014). Abiotic processes, such as the water-rock reaction of serpentinization, fuel and sustain microbial communities in sediments and rocks exposed at the seafloor and in the subsurface of the ocean crust (Kelley 2005). Other such abiotic drivers of life in the deep subsurface include radiolytic H_2 production (Blair et al. 2007) and hydrocarbon 'cracking' (Horsfield et al. 2006). Diverse chemosynthetic metabolisms are employed by the deep biosphere, taking advantage of these abiotic processes, including H_2 oxidation, SO_4^{2-} reduction, CH_4 oxidation, methanogenesis, O_2 reduction, organic carbon degradation, and Mn reduction (Orcutt et al. 2013).

Serpentinization, the water-rock reaction forming serpentine mineral assemblages from olivine and pyroxene-bearing protoliths, can co-occur with the production of hydrogen, methane, and diverse organic compounds (McCollom and Seewald 2013). Natural waters impacted by serpentinization are often Ca^{2+}- or Mg^{2+} - rich (Neal 1984; Paukert et al. 2012), thus appropriate for carbonate precipitation, including in ophiolite

1

groundwater flow systems and travertine-producing seeps/springs. Serpentinization is regarded as a geologic process important to the sustainability of the deep biosphere (Schrenk et al. 2013) and the origin of life (Russell et al. 2010; Sleep et al. 2011). Ongoing research identifies the following specific metabolic reactions as relevant to deep life in serpentinites: anaerobic CO-oxidation, acetogenesis, reduction of sulfur compounds, H_2 oxidation, CO_2 fixation, magnetite reduction, and fermentation (Crespo-Medina et al. 2014; Miller et al. 2016; Rowe et al. 2017; Twing et al. 2017).

Carbonate minerals result also from spring deposits fed by serpentinizing waters at continental sites; serpentinite-associated travertines are well known (Barnes and Oneil 1971; Flinn and Pentecost 1995) with implications for Mars-related serpentinization (Szponar et al. 2013) and CO_2 sequestration via travertine formation (Kelemen and Matter 2008; Paukert et al. 2012). These travertines have the potential to lock in organic material and preserve it over time, recording changing community characteristics. Co-registered mineral and organic analytical data are needed to test for robust detection and discernment of closely associated mineral and organic phases: careful application of Fourier Transform Infrared (FTIR) Spectroscopy has potential to answer this need.

μFTIR relies upon coupling classic petrographic microscopy with FTIR Spectroscopy. μFTIR is used in a wide range of environmental studies on microbial ecology (Wenning et al. 2002; Igisu et al. 2006, 2009), and in recent projects, μFTIR has been used to identify bacteria even down to strain level (Igisu et al. 2012) in pure cultures. Here, we describe the application of μFTIR to mapping minerals and related organics in polished rock/mineral samples of serpentinization-related lithologies. Specifically, we provide Attenuated Total Reflection FTIR (ATR-FTIR), reflection

mode-µFTIR (R-FTIR), and transmission mode-µFTIR (T-FTIR) profiles for phases important in (I) serpentinites and selected associated minerals (serpentinite, peridotite, pyroxenite; olivine, pyroxene, serpentine, magnetite, brucite) (ATR- and R-FTIR) and embedded organics (T-FTIR), (II) travertine and selected constituent minerals (carbonate crusts; calcite, dolomite) (ATR- and R-FTIR) and (III) a polysaccharide proxy for exopolysaccharides (EPS) (ATR- and R-FTIR). We also present the preliminary findings of a serpentinite incubation experiment; we incubated polished wafers of serpentinite collected from the Coast Range Ophiolite Microbial Observatory (CROMO) in well water, collected from a high pH (11.5) CROMO priority well in the Quarry Valley (QV) (well ID QV1,1). The QV 1,1 well hosts a chemosynthetically diverse microbial community due to the reducing conditions maintained by serpentinization (Cardace et al. 2013; Crespo-Medina et al. 2014; Twing et al. 2017). Lastly, we evaluated the resolving power of µFTIR for the detection of mineral-encapsulated, residual organic compounds from biological activity by mixing increasing mass proportions of xanthan gum (x.g.) in a ground serpentinite matrix, obtained during drilling of CROMO. We describe new findings, using µFTIR to map minerals and associated organics related to serpentinization.

METHOD

We prepared specimens as polished solid wafers and/or homogenized powders. We identified, confirmed, and documented FTIR wavenumber (cm^{-1}; aka IR frequency) regions linked to (I) serpentinization-associated minerals and embedded organics, (II) carbonate-associated minerals, and (III) a polysaccharide proxy for EPS. In all cases, we

referenced observed IR spectra to published findings (Hunt and Salisbury 1974; Lafuente et al. 2015), supported by X-ray diffraction results. ATR-FTIR is able to analyze powders, solids, and liquids with little sample preparation. The sample is placed on a crystal window (we use diamond), and an IR beam is directed onto the crystal, and attenuates through the crystal as an evanescent wave, which comes into contact with the sample at each bounce; the resulting wavelengths are read by the detector as an interferogram (Figure 1) (Thermo Scientific 2013). μFTIR involves a more strenuous solid sample preparation by needing a flat sample; to analyze rock samples, polishing is necessary. R-FTIR requires a flat, polished surface and works by emitting an IR beam on the surface of the sample and detecting the wavelengths that were reflected off of the surface (Figure 2) (Thermo Scientific 2013). T-FTIR requires a thin doubly polished sample and works by emitting an IR beam through a thin sample and detecting the transmitted wavelengths (Figure 3) (Thermo Scientific 2013).

Sample preparation

For μFTIR (R- and T-FTIR), we polished peridotite, serpentinite, and carbonate samples from various locations (Table 1), with polishing protocol as described previously (Lowenstern and Pitcher 2013). In brief, wafers were ground to < 500 μm thickness for R-FTIR analysis and to <100 μm thickness for T-FTIR while fixed to a round glass slide, and polished using increasingly fine polishing papers and diamond paste suspensions. For ATR-FTIR and X-ray diffraction (XRD), we powdered splits of these samples, and passed through a 100-mesh (150 μm pore size) sieve to work with a standardized <150 μm size fraction. More detail is provided below.

R-FTIR

We used a Thermo Nicolet iS50 FTIR spectrometer coupled with a Continuum IR microscope to map minerals in R-FTIR (King and Larsen 2013), using a MCT-A (mercury cadmium telluride) detector and KBr beamsplitter, with 100x100 μm beam aperture, 64 scans, and 4 cm^{-1} resolution. Background data were collected on polished gold. We collected sample points on individual minerals on each polished wafer to provide representative spectra of each mineral. We also mapped serpentinite and travertine wafers with autofocus at each sample point in R-FTIR using the Omnic Atlμs software, and produced frequency heat maps to differentiate regions with different bond characteristics. For maps, we used a 25x25 μm beam aperture, scanning sample points at 25 μm intervals, with 128 scans and 4 cm^{-1} resolution at each sample point.

T-FTIR

We used the same instrument, detector, beamsplitter, and mapping settings as R-FTIR to map a CROMO serpentinite wafer (SRP-1) using T-FTIR.

Attenuated total reflectance FTIR

We analyzed powdered splits of rock/mineral samples via ATR-FTIR (Lowenstern and Pitcher 2013), using the same unit, same settings, and diamond window. Background data were collected on air.

XRD

We confirmed mineral identification of powdered splits via X-ray diffraction using Olympus Terra XRD unit (Blake et al. 2012) outfitted with a Co tube. Operating parameters for this instrument are set to 250 exposures. Peak identification was facilitated using the XPowder (http://www.xpowder.com/) peak-matching software.

Incubation experiment

Serpentinite-hosted well water was collected directly from the scientific monitoring well at the Coast Range Ophiolite Microbial Observatory (CROMO) Quarry Valley 1,1 well (Cardace et al. 2013) in January, 2016, by pumping water into a cleaned polypropylene slide staining jar, fitted with polished serpentinite samples attached to glass slides. The closed jar remained at ambient laboratory temperature (~21ºC) for 3 weeks, followed by 4 weeks in a standard refrigerator to inhibit growth, prior to analysis. Incubated wafer surfaces were analyzed by R-FTIR with standard reflection mode settings as above, and re-analyzed after surface cleaning with isopropanol.

Limit of detection assay for polysaccharides

We mixed pulverized serpentinite matrix (<150 μm fraction) obtained during CROMO drilling (Cardace et al. 2013) with xanthan gum (xanthan gum obtained commercially) in increasing proportions: 0, 0.001, 0.005, 0.01, 0.05, 0.1, 1, 2, 5, 20, 50, 80, 95, 98, 99, 99.9, and 100 wt. % x.g. to simulate trace biofilm EPS presence and dense EPS biofouling of mineral matrices. Mixtures were made gravimetrically, using an analytical balance, and homogenized by shaking prior to analytical work. Xanthan gum

mixtures were analyzed by ATR-FTIR, with 128 scans and 8 cm^{-1} resolution (inverse centimeters, also called wavenumbers, is equivalent to the infrared frequency).

In addition, we made a homogenous 2 g/L solution of xanthan gum and DI water and applied drops onto a polished serpentinite wafer (CROMO surface serpentinite sample). After a film formed, the polysaccharide-coated wafer was analyzed on and off the xanthan gum film with R-FTIR using standard reflection mode settings with the background collected on polished gold.

RESULTS

Confirmation of applicability of R-FTIR, ATR-FTIR and T-FTIR to serpentinites and travertines

Figures 3 through 8 (and appendix figures 1-9) show the bulk ATR-FTIR spectra and R-FTIR spectra of the minerals identified in each of the samples (Table 1); minerals identified by cross-referencing spectra are listed in parentheses.

In general, we determined major components of the mineralogy using ATR-FTIR with reference to the RRUFF database (Lafuente et al. 2015). ATR-FTIR mode was able to resolve the minerals in highest concentration in the powder splits. For example, serpentinite from New Zealand was analyzed in ATR-FTIR and R-FTIR; for this sample, the ATR-FTIR spectrum (Figure 4) revealed the presence of only lizardite, whereas R-FTIR data indicated the presence of pyroxene and magnetite also. Sometimes, there are peaks in the ATR-FTIR spectra that are very clearly different minerals. For example, the serpentinite from Jade Mountain Lodge (Figure 5) clearly shows the presence of both lizardite (3682 cm^{-1}, 930 cm^{-1} and 600 cm^{-1}) and carbonate (1383 cm^{-1}, 870 cm^{-1}, and 711

7

cm^{-1}). Sometimes, however, when there are multiple minerals represented in the spectra, identifying all of the minerals can be difficult due to peak overlap. For example, the ATR-FTIR spectrum for olivine (OL-1; Figure 7) shows strong olivine (forsterite) peaks, however, there is a peak at 3680 cm^{-1}, which may indicate the presence of serpentine. Given this peak, it is likely that the shoulder of the strongest forsterite peak at 930 cm^{-1} is due to serpentine as well; the presence of lizardite would also account for the constructive interference at 600 cm^{-1} since this peak occurs in both forsterite and lizardite.

R-FTIR is useful in observing minerals individually on a polished surface, whereas ATR-FTIR identifies the minerals of highest concentration in the bulk powder. R-FTIR provides spectra with similar shape and relative peak height to the ATR-FTIR reference spectra (as in Lafuente et al., 2015). There is, however, common occurrences of peak shifts compared to ATR-FTIR as a result of the refractive indices changing the reflected light at each subsequent layer (medium) absorbing light (Spragg 2013); for example, the serpentine peaks of the serpentinite from CROMO are 930 cm^{-1} and 600 cm^{-1} in ATR-FTIR mode and are 947 cm^{-1} and 642 cm^{-1} in R-FTIR. R-FTIR spectra were affected by the quality of the polish and the texture of the sample. When the IR aperture beam interacted with pores or if the sample was not completely perpendicular to the beam (as is the case for subtle roughness in imperfectly polished surfaces), the signal to noise ratio (S:N) decreased, and the top of spectral peaks were skewed in shape. For example, the peridotite from New Zealand (PER-1; Figure 6) shows forsterite (an olivine mineral) represented as the most abundant mineral in the sample by ATR-FTIR; with R-FTIR, olivine can be identified, but the top of the relevant peaks are rounded and skewed inwards. It may be that there is another mineral (*e.g.,* pyroxene) just below the surface

that the beam is able to reach. A trace amount of an additional mineral (*e.g.,* finely dispersed serpentine or iron oxyhydroxides) may be present on the surface, but not as a visually distinguishable grain at the scale of analysis, on the surface of the sample.

Analyses of dolomite (Figure 8) provide an example of how R-FTIR can result in both peak shifting and altered peak shapes. Peaks in ATR-FTIR mode line up with reference dolomite (RRUFF, Lafuente et al., 2015) at 1413 cm^{-1}, 873 cm^{-1}, and 727 cm^{-1}; in R-FTIR, these peaks shift to 1494 cm^{-1}, 897 cm^{-1}, and 727 cm^{-1}. XRD and visual inspection of the sample confirm dolomite. Despite differences in the ATR-FTIR and R-FTIR spectra, the data represent dolomite. Another example of altered peak shape is evident in analyses of optical calcite (Figure 9), which is clearly identifiable in reference spectra (Lafuente et al. 2015), although the peaks were skewed as a result of how the light interacted with the sample, a classic characteristic of optical calcite (Valenzano et al. 2007).

A principle component analysis (using JMP$^®$) of ATR-FTIR spectra was conducted by including all wavenumber and intensity data (7000+ data points) from each sample (Figure 12). Principle component 1 (PC 1) appears to separate spectra based on overall intensity of the spectrum; for example, MAG-1 pointing left has a much higher spectrum than other samples (Appendix Figure 6). PC 2 seems to separate the spectra by peak location; therefore, the samples are separated by lithologic type: ultramafics are located in the top right and carbonates in bottom right. SRP-3 and TRAV-WS are located in between the extremes as a result of having both carbonate and Si-O bonds.

With R-FTIR frequency heat maps, we are able to parse FTIR data using peaks that are diagnostic for specific minerals (Figure 10 &11). Frequency heat maps of

serpentinite from CROMO (id SRP-1), based on the diagnostic peaks for serpentine at 976 cm^{-1} (Si-O) and for magnetite at 680 cm^{-1} (Figure 10B and C, respectively), highlight areas of highest intensities (absorbance) at those wavenumber regions in bluer tones, and areas of lower intensities in redder tones. The heat map of 976 cm^{-1} effectively highlights the magnetite-rich region in red, which does not have a distinguishable peak or elevated absorbance at 976 cm^{-1} (that is, serpentine does not co-occur with magnetite at this scale) (Figure 10). Where there is serpentine, you can discern areas richer in the Si-O bond, such as the darkest blue vein, correlated with the light-colored, late-stage serpentine vein, seen in Figure 10A. In contrast, the heat map of 680 cm^{-1} highlights the serpentine-rich regions in red, which do not contain magnetite, and highlights the magnetite-rich regions in yellow, green, and blue tones.

A frequency heat map of a travertine thin section from CROMO (id TRAV-WS3G) was made to target the wavenumber region related to the Si-O bond (1020 cm^{-1}; Figure 11). Microprobe data for elemental Si show bands of high Si throughout a manually polished companion sample (microprobe images in Appendix Figure 11; heat map images of companion sample in Appendix Figure 10); Si-O bonds are thus expected within the $CaCO_3$–dominated matrix. The heat map highlights Si-O bond occurrence in blue, a representation of the optically clear area between the black and red areas (Figure 11). The black mineral region has low intensity carbonate peaks at 1410 cm^{-1} and 884 cm^{-1} with the strongest peak at 1538 cm^{-1}, which is related to the ferrocyanide staining on this sample (C-N and/or H-N), used to flag ferrous iron-rich regions in this thin-section. The red-shaded mineral region has low intensity peaks representing Si-O and a strong

peak at 1556 cm^{-1}. The clear area to the left is a pore in the sample and has low intensity glue and glass peaks in this region.

A frequency T-FTIR area map of a serpentinite (SRP-1) doubly polished wafer was created to assess the ability of T-FTIR to detect embedded organics with a strong mineral background. With this map, we found an increase in intensity in C-H bond wavenumber regions (~2900 cm^{-1}) and in O-H, and amide (Amide 1: C=O, Amide 2: CNH) wavenumber regions (~1600 cm^{-1}) (Figure 13D) near areas rich in magnetite. By conducting a PCA heat map, in the Omnic Atlμs software, we could select the peak area regions on which to base the PCA. Choosing the 2900 cm-1 (3000-2830 cm-1) and 1600 cm-1 (1800-1500 cm-1) peak areas for PCA provided a first principle component (PC1) that controls 92% of the variance, and is based on regions that have higher peak areas at both the 2900 cm-1 and 1600 cm-1 wavenumber regions (Figure 13C); a PCA heat map of PC1 highlights all regions on and surrounding magnetite (Figure 13B). By extracting a line map from the area map (red line in Figure 13A extracted as a heat map in Figure 13D), we observe an overall spectral elevation when the IR beam is overlying magnetite (the black area about half way up the line), which is a result of magnetite being opaque; and we can also see increases of the 2900 cm^{-1} and 1600 cm^{-1} regions at and near the magnetite and tapering off away from the magnetite vein.

Assessment of FTIR-based resolution of organic films on serpentinites: Pilot Incubation Experiment

R-FTIR data were collected on a transect of a CROMO serpentinite sample (SRP-1) after incubation in naturally occurring groundwaters (from CROMO Quarry Valley 1,1

scientific monitoring well; Figure 14A) The line map was taken before (Figure 14B) and after (Figure 14C) cleaning with isopropyl alcohol; all sample points on the transect show very similar spectra before cleaning and again after cleaning; therefore, one representative spectrum was selected for before and after cleaning. Before cleaning the surface, the spectra show a strong serpentine signal with a broad, low intensity background noise from 1200 cm^{-1} to 2500 cm^{-1}. After cleaning the surface, the spectra show a strong serpentine signal with little background noise, likely as a result of the instrument warming up over time.

Assessment of FTIR-based resolution of surface films/embedded organic loads related to serpentinites: Constraining the limit of detection for a representative polysaccharide

Xanthan gum (exopolysaccharide of *Xanthamonas campestris*) serves in this study as a proxy for biologically produced exopolysaccharides, and data confirm that incipient biofilm formation can be tracked using FTIR. Xanthan gum represents several of the organic bonds that would be found if a biofilm developed on the surface of a rock (Figure 15), including O-H, C-H, C=O, Carboxylate groups, acetate groups and C-O (Osiro et al. 2011). We used R-FTIR to contrast relevant spectral regions on a serpentinite wafer with and without xanthan gum film (Figure 16). Data collected on the xanthan gum film show medium intensity peaks associated with xanthan gum and strong intensity peaks associated with serpentine in the underlying rock matrix (Figure 16C). When compared to data collected on serpentinite without the xanthan gum film, the intensity of the serpentine peaks was greater (higher) on the xanthan gum-free area; the

intensity of the serpentine peaks was lesser (damped) on the xanthan gum-coated area. A PCA of data points along a transect from on the xanthan gum film (Figure 16A point #1) to off the xanthan gum film (Figure 16A point #29) separate spectra that are on and off the xanthan gum film (Figure 16B).

For the set of synthetic mixtures with increasing xanthan gum proportions in pulverized serpentinite, analyzed using ATR-FTIR, we used an O-H angular deformation peak at 1600 cm^{-1} to determine the presence of xanthan gum because 1) there are no overlapping mineral peaks in this region, and 2) the peak is narrower and higher in intensity when compared to other peaks free of overlapping mineral peaks. Thus, the 1600 cm^{-1} peak can be detected most easily at low concentrations. When observing the entire spectra (Figure 17A), the 1600 cm^{-1} peak emerges at 5 wt. % xanthan gum; the pure serpentinite powder and low xanthan gum concentration mixtures have a peak at 1630 cm^{-1} with a shoulder peak at 1555 cm^{-1}, both of which may relate to organics/biomass intrinsic to the rock matrix itself (Figure 17B). Spectral data for mixtures with concentrations below 20 wt. % xanthan gum maintain a clear signal for serpentine in that region; however, at 0.1 wt. % xanthan gum, a change in peak shape is distinguishable from lower concentrations, where the baseline is smoother and the 1630 cm^{-1} peak is shifted towards lower wavenumbers. Peak height, area and location were recorded for every mixture (Figure 18-20). There is constructive interference at this region by other bonds at 1630 cm^{-1}; the peak height still increases as the peak shifts from 1630 cm^{-1} to 1600 cm^{-1} with increasing xanthan gum concentration at a constant rate (R^2 = 0.9947; Figure 18A). Even at low concentrations (at least by 1 wt %), there is a consistent increase in peak height in the 1630 cm^{-1} to 1600 cm^{-1} region (Figure 18B).

Peak area of the 1775-1500 cm^{-1} region also increases at a constant rate (R^2 = 0.99405; Figure 19A), and again, at low concentrations (at least by 1 wt %), there is a consistent increase in peak area (Figure 19B). Peak location, as previously mentioned, shifts towards lower wavenumbers with increasing xanthan gum concentration in a logarithmic rate (R^2 = 0.79656; Figure 20A). There are outliers, such as 0.05 and 0.1 wt %, that occur in all three measurements; the reason may be that this range of concentrations is at a threshold with increased xanthan gum so that it experiences constructive interference with nearby peaks, causing a baseline shift, and thereby shifting all of the measurements. It also may be the case that the aliquot of serpentinite for that sample started with fewer organics.

DISCUSSION

Suitability of FTIR for phase discrimination in serpentinites and travertines

ATR-FTIR

ATR-FTIR, a method that is widely available, provides a bulk reading of dominant minerals in powdered rock/mineral samples. ATR-FTIR is able to differentiate the serpentine (~980 cm^{-1} and 3700 cm^{-1}), olivine (~860 cm^{-1}), pyroxene (multiple sharp peaks between 1060 cm^{-1} and 620 cm^{-1}), and magnetite (~660 cm^{-1}) individually with ease based on relative peak shape and location (Table 2). However, it is difficult to distinguish the subcategories of minerals (*i.e.*, the serpentine minerals, antigorite and lizardite) because the bonds and their relative abundances (on which FTIR data are based) are very similar. ATR-FTIR is also able to distinguish between the carbonate (~1400, cm^{-1} 870 cm^{-1} and 730 cm^{-1}) and silicon-rich layers (1020 cm^{-1}) in travertine

(Table 2; Figure 11), although, again, differentiating the carbonate minerals presents a challenge because the bonds and their relative abundances are similar.

The main issue encountered with ATR-FTIR is the ability to distinguish peak overlap of different minerals in the bulk-powdered sample, in addition to its overall decreased sensitivity compared to µFTIR. One needs to be familiar with relative mineral peak location and shape to identify multiple minerals within the bulk, powdered reading.

As a result of this pilot study, it is clear that we need to develop a standardized, robust statistical treatment of peak locations that can help us interpret complex samples.

R-FTIR

R-FTIR is capable of differentiating adjacent minerals and individual grains greater or equal to the aperture size of the IR beam (between 25x25 µm to 150x150 µm). The higher resolution afforded by R-FTIR data allows direct probing of sample characteristics. However, there may be peak shifting issues with R-FTIR; one must consider the possibility of constructive interference of the presence of other minerals in the sample point region. The shape and relative peak locations will likely handle peak shifting; however, a correction (Kramer's Kronig correction), may be very useful addressing minor peak shifts (Spragg 2013).

Frequency heat maps are useful in highlighting specific aspects of rich spectral data sets, as when searching for a mineral that has a distinct spectral peak relative to adjacent minerals. If spectra have a low S:N, low intensity trace mineral or organic peak variations may not be resolvable, even with this method.

For microbiology, R-FTIR is a useful tool in observing changing organic bonds across spatial boundaries with high resolution, specifically to analyse microbial biofilms grown on varying nutrient conditions (Chen et al. 2013). Other environmental studies have used R-FTIR to observe phases in rocks, such as coal and shale (Chen et al. 2015)

T-FTIR as a tool for detecting embedded organics at mineral boundaries

T-FTIR, although involving strenuous sample preparation, is a valuable tool in detecting naturally occurring organics embedded in rocks and observing mineral associations of organics. In this study, we found an increase of aliphatic C-H (~2900 cm^{-1}), O-H (~1630 cm^{-1}), and potentially protein-related bonds (Amide I and II; 1550-1650 cm^{-1}) near magnetite-rich regions. It is difficult to determine using FTIR, whether there are whole cells embedded near magnetite, or if there are shreds of microbes (lipids, proteins, etc.) left over from being trapped during mineral formation. Pairing FTIR with other techniques, such as SEM and Raman would be helpful in determining the organic components. In other words, important discrimination between structurally similar phases (such as in the carbonates) must rely on complementary, co-registered chemical analyses at the same scale, and finer resolution of organic compound type (full identification and possibly compound-specific isotopic characteristics) will strengthen the interpretive power of this analytical approach.

Microbiology studies that involve T-FTIR typically include stamping or drying a film of bacterial colonies on an IR transparent plate (Igisu et al. 2012; Faghihzadeh et al. 2016). In other environmental studies, thin wafers of rocks are analyzed to observe volatile inclusions, such as H_2O and CO_2 in rocks (Lowenstern and Pitcher 2013).

Similarly to this study, another study has used T-FTIR to observe prokaryotic microfossils embedded in chert (Igisu et al. 2006). This study combines these T-FTIR utilities to observe naturally occurring biogenic organics, such as lipid and protein microbial debris in rocks related to serpentinization, a process that fuels life on Earth.

FTIR spectroscopy as a tool for resolving organic loads on/in Earth materials

It is unclear whether short duration incubations (~3 weeks' duration) produce enough adhered biomass/organic materials to be well resolved by FTIR approaches. However, analyses of synthetic mixtures of serpentinite and xanthan gum do reflect changing intensity of the 1600 cm^{-1} peak, a peak related to polysaccharides (Osiro et al. 2011) in a wavenumber region unhindered by mineral peak interferences. We show that xanthan gum is detectable in the range of expected organic load in serpentinites (total carbon @ 0.001 to 0.1 %, equivalent to 10 to 1000 ppm total carbon, respectively) (Alt et al. 2012). FTIR thus has the capability to detect low, geologically relevant concentrations of organic material in natural serpentinites. Diagnostic FTIR peaks for organics as carbohydrates, DNA, lipids, and proteins (Maquelin et al. 2002; Osiro et al. 2011; Igisu et al. 2012) should be used in regions where mineral peaks do not overlap: the strongest minerals peaks are typically in the 1400-500 cm^{-1} range – identifying the minerals first and then searching for lower-intensity biomarker peaks in other wavenumber regions allows for best accuracy. Statistical treatment of xanthan gum mixtures' peak locations and intensities can help us interpret natural serpentinites.

CONCLUSIONS

The findings of this study indicate that organic presence with a mineral background can be detected using FTIR. Implications for this study include the ability to detect and map polished rock surfaces to determine the association of organics to mineral phases and boundaries in serpentinization-related lithologies. Future directions include analyzing polished rock and mineral wafers before and after incubation in serpentinite-hosted natural waters *in situ*, differentiating signatures of surface biofilms (via R-FTIR) from embedded/preserved organics (via T-FTIR), and cross-referencing organic-rich regions in natural samples with other analytical techniques (*e.g.*, Raman spectroscopy). As a result of this study, we confirm the applicability of FTIR-based techniques in micro-scale investigations of organics in ultramafic and carbonate rocks, and we establish the need for an integrated database covering mineral and organic compounds.

ACKNOWLEDGEMENTS

REFERENCES CITED

Alt, J.C., Garrido, C.J., Shanks, W.C., Turchyn, A., Padrón-Navarta, J.A., López
   Sánchez-Vizcaíno, V., Gómez Pugnaire, M.T., and Marchesi, C. (2012) Recycling
   of water, carbon, and sulfur during subduction of serpentinites: A stable isotope

study of Cerro del Almirez, Spain. Earth and Planetary Science Letters, 327–328, 50–60.

Barnes, I., and Oneil, J. (1971) Calcium-magnesium carbonate solid solutions from Holocene conglomerate cements and travertines in the Coast Range of California.

Blair, C.C., D'Hondt, S., Spivack, A.J., and Kingsley, R.H. (2007) Radiolytic hydrogen and microbial respiration in subsurface sediments. Astrobiology, 7, 951–970.

Blake, D., Vaniman, D., Achilles, C., Anderson, R., Bish, D., Bristow, T., Chen, C., Chipera, S., Crisp, J., Des Marais, D., and others (2012) Characterization and calibration of the CheMin mineralogical instrument on Mars science laboratory. Space Science Reviews, 170, 341–399.

Cardace, D., Hoehler, T., McCollom, T., Schrenk, M., Carnevale, D., Kubo, M., and Twing, K. (2013) Establishment of the Coast Range ophiolite microbial observatory (CROMO): drilling objectives and preliminary outcomes. Scientific Drilling, 16, 45–55.

Chen, Y., Zou, C., Mastalerz, M., Hu, S., Gasaway, C., and Tao, X. (2015) Applications of micro-fourier transform infrared spectroscopy (FTIR) in the geological sciences—A Review. International Journal of Molecular Sciences, 16, 30223–30250.

Chen, Y.P., Zhang, P., Guo, J.S., Fang, F., Gao, X., and Li, C. (2013) Functional groups characteristics of EPS in biofilm growing on different carriers. Chemosphere, 92, 633–638.

Colwell, F.S., and D'Hondt, S. (2013) Nature and extent of the deep biosphere. Reviews in Mineralogy and Geochemistry, 75, 547–574.

Crespo-Medina, M., Twing, K.I., Kubo, M.D.Y., Hoehler, T.M., Cardace, D., McCollom, T., and Schrenk, M.O. (2014) Insights into environmental controls on microbial communities in a continental serpentinite aquifer using a microcosm-based approach. Frontiers in Microbiology, 5.

D'Hondt, S., Spivack, A.J., Pockalny, R., Ferdelman, T.G., Fischer, J.P., Kallmeyer, J., Abrams, L.J., Smith, D.C., Graham, D., Hasiuk, F., and others (2009) Subseafloor sedimentary life in the South Pacific Gyre. Proceedings of the National Academy of Sciences, 106, 11651–11656.

Faghihzadeh, F., Anaya, N.M., Schifman, L.A., and Oyanedel-Craver, V. (2016) Fourier transform infrared spectroscopy to assess molecular-level changes in microorganisms exposed to nanoparticles. Nanotechnology for Environmental Engineering, 1, 1.

Flinn, D., and Pentecost, A. (1995) Travertine-cemented screes on the serpentinite seacliffs of Unst and Fetlar, Shetland. Mineralogical Magazine, 59, 259–265.

Horsfield, B., Schenk, H., Zink, K., Ondrak, R., Dieckmann, V., Kallmeyer, J., Mangelsdorf, K., Diprimio, R., Wilkes, H., and Parkes, R. (2006) Living microbial ecosystems within the active zone of catagenesis: Implications for feeding the deep biosphere. Earth and Planetary Science Letters, 246, 55–69.

Hunt, G.R., and Salisbury, J.W. (1974) Mid-infrared spectral behavior of igneous rocks. Environmental Research Papers, 74, 1–142.

Igisu, M., Nakashima, S., Ueno, Y., Awramik, S.M., and Maruyama, S. (2006) In situ infrared microspectroscopy of ~850 million-year-old prokaryotic fossils. Applied Spectroscopy, 60, 1111–1120.

Igisu, M., Ueno, Y., Shimojima, M., Nakashima, S., Awramik, S.M., Ohta, H., and Maruyama, S. (2009) Micro-FTIR spectroscopic signatures of Bacterial lipids in Proterozoic microfossils. Precambrian Research, 173, 19–26.

Igisu, M., Takai, K., Ueno, Y., Nishizawa, M., Nunoura, T., Hirai, M., Kaneko, M., Naraoka, H., Shimojima, M., Hori, K., and others (2012) Domain-level identification and quantification of relative prokaryotic cell abundance in microbial communities by Micro-FTIR spectroscopy. Environmental Microbiology Reports, 4, 42–49.

Jorgensen, B.B. (2012) Shrinking majority of the deep biosphere. Proceedings of the National Academy of Sciences, 109, 15976–15977.

Kelemen, P.B., and Matter, J.M. (2008) In situ carbonation of peridotite for CO2 storage. Proceedings of the National Academy of Sciences, 105, 17295–17300.

Kelley, D.S. (2005) A serpentinite-hosted ecosystem: The Lost City Hydrothermal Field. Science, 307, 1428–1434.

King, P.L., and Larsen, J.F. (2013) A micro-reflectance IR spectroscopy method for analyzing volatile species in basaltic, andesitic, phonolitic, and rhyolitic glasses. American Mineralogist, 98, 1162–1171.

Lafuente, B., Downs, R.T., Yang, H., and Stone, N. (2015) The power of databases: The RRUFF project, 1-29 p. Highlights in Mineralogical Crystallography.

Lowenstern, J.B., and Pitcher, B.W. (2013) Analysis of H2O in silicate glass using attenuated total reflectance (ATR) micro-FTIR spectroscopy. American Mineralogist, 98, 1660–1668.

Maquelin, K., Kirschner, C., Choo-Smith, L.-P., van den Braak, N., Endtz, H.P.,

Naumann, D., and Puppels, G.J. (2002) Identification of medically relevant microorganisms by vibrational spectroscopy. Journal of microbiological methods, 51, 255–271.

McCollom, T.M., and Seewald, J.S. (2013) Serpentinites, hydrogen, and life. Elements, 9, 129–134.

Miller, H.M., Matter, J.M., Kelemen, P., Ellison, E.T., Conrad, M.E., Fierer, N., Ruchala, T., Tominaga, M., and Templeton, A.S. (2016) Modern water/rock reactions in Oman hyperalkaline peridotite aquifers and implications for microbial habitability. Geochimica et Cosmochimica Acta, 179, 217–241.

Neal, C. (1984) Calcium and magnesium hydroxide precipitation from alkaline groundwaters in Oman, and their significance to the process of serpentinization. Mineralogical Magazine, 48, 237–241.

Orcutt, B.N., LaRowe, D.E., Biddle, J.F., Colwell, F.S., Glazer, B.T., Reese, B.K., Kirkpatrick, J.B., Lapham, L.L., Mills, H.J., Sylvan, J.B., and others (2013) Microbial activity in the marine deep biosphere: Progress and prospects. Frontiers in Microbiology, 4, 1–15.

Osiro, D., Franco, R.W.A., and Colnago, L.A. (2011) A spectroscopic characterization of the exopolysaccharide of Xanthomonas axonopodis pv. citri in Cu 2+ Resistance Mechanism. Article J. Braz. Chem. Soc, 22, 1339–1345.

Parkes, R.J., Cragg, B., Roussel, E., Webster, G., Weightman, A., and Sass, H. (2014) A review of prokaryotic populations and processes in sub-seafloor sediments, including biosphere:geosphere interactions. Marine Geology, 352, 409–425.

Paukert, A.N., Matter, J.M., Kelemen, P.B., Shock, E.L., and Havig, J.R. (2012) Reaction

path modeling of enhanced in situ CO2 mineralization for carbon sequestration in the peridotite of the Samail Ophiolite, Sultanate of Oman. Chemical Geology, 330–331, 86–100.

Rowe, A., Yoshimura, M., LaRowe, D., Bird, L., Amend, J., Nealson, K., and Okamoto, A. (2017) In situ electrochemical enrichment and isolation of a magnetite-reducing bacterium from a high pH serpentinizing spring. Environmental microbiology, 1–41.

Russell, M.J., Hall, A.J., and Martin, W. (2010) Serpentinization as a source of energy at the origin of life. Geobiology, 8, 355–371.

Schrenk, M.O., Brazelton, W.J., and Lang, S.Q. (2013) Serpentinization, carbon, and deep life. Reviews in Mineralogy and Geochemistry, 75, 575–606.

Sleep, N.H., Bird, D.K., and Pope, E.C. (2011) Serpentinite and the dawn of life. Philosophical Transactions of the Royal Society B: Biological Sciences, 366, 2857–2869.

Spragg, R. (2013) Reflection measurements in IR spectroscopy. Reflection Measurements in IR Spectroscopy.

Szponar, N., Brazelton, W.J., Schrenk, M.O., Bower, D.M., Steele, A., and Morrill, P.L. (2013) Geochemistry of a continental site of serpentinization, the Tablelands Ophiolite, Gros Morne National Park: A Mars analogue. Icarus, 224, 286–296.

Thermo Scientific (2013) Introduction to FT-IR Sample Handling. Thermo Fischer Scientific, Inc.

Twing, K.I., Brazelton, W.J., Kubo, M.D.Y., Hyer, A.J., Cardace, D., Hoehler, T., McCollom, T.M., and Schrenk, M.O. (2017) Serpentinization-influenced groundwater harbors extremely low diversity microbial communities adapted to high

pH. Frontiers in Microbiology, 8, 308.

Valenzano, L., Noël, Y., Orlando, R., Zicovich-Wilson, C.M., Ferrero, M., and Dovesi, R. (2007) Ab initio vibrational spectra and dielectric properties of carbonates: Magnesite, calcite and dolomite. Theoretical Chemistry Accounts, 117, 991–1000.

Wenning, M., Seiler, H., and Scherer, S. (2002) Fourier-transform tnfrared microspectroscopy, a novel and rapid tool for identification of yeasts. Applied and Environmental Microbiology, 68, 4717–4721.

LIST OF FIGURE CAPTIONS

Table 1. Listed are the ultramafic and carbonate samples that were prepared for R-FTIR, ATR-FTIR, and supporting XRD data.

Table 2. Listed are the descriptions of the RRUFF mineral peaks we used to identify our samples via ATR-FTIR and R-FTIR. Bond assignments are not included, as most peaks present are in the fingerprint region of the infrared spectrum, where bonds represent the complex molecules rather than by single bonds.

Figure 1. Multi-bounce and single bounce beams through a sample occurring via ATR-FTIR as an evanescent wave passes through an ATR-FTIR crystal (Thermo Scientific 2013).

Figure 2. The principle of R-FTIR is presented visually, showing the IR beam bouncing off the only the surface of a sample at an angle based on the material's refractive index (true specular reflectance) and an instance where some of the energy of the beam passes through the surface of the sample and reflects off the underlying substrate (reflection-absorption) (Thermo Scientific 2013).

Figure 3. T-FTIR involves the transmission of the IR beam through a flat sample surface and the transmitted light is measured by the detector, as shown in the figure (Thermo Scientific 2013).

Figure 4. ATR-FTIR and R-FTIR spectra of serpentinite from Poon Bato, Philippines (SRP-2).

Figure 5. ATR-FTIR and R-FTIR spectra of serpentinite from Jade Mountain Lodge, Crescent City, CA (SRP-3).

Figure 6. ATR-FTIR and R-FTIR spectra of peridotite from Lake Ronald, New Zealand (PER-1).

Figure 7. ATR-FTIR and R-FTIR spectra of olivine (OL-1).

Figure 8. ATR-FTIR and R-FTIR spectra of dolomite from Sussex County, NJ (DOL-1).

Figure 9. ATR-FTIR and R-FTIR spectra of optical calcite from Iceland (CAL-1).

Figure 10. A) An R-FTIR area map of serpentinite (SRP-1) includes a magnetite grain (red star) surrounded by lizardite (blue star). B) A frequency heat map of 976 cm^{-1}, a wavenumber indicative of serpentine, shows higher intensity in blue and green tones where serpentine is present. C) A frequency heat map of 680 cm^{-1}, a wavenumber indicative of magnetite, shows higher intensity in blue and green tones where magnetite is present. D and E) Spectra of representative serpentine (blue star) and magnetite (red star) are presented with a solid vertical line noting the location of the 976 cm^{-1} region and a dashed vertical line noting the location of the 680 cm^{-1} region.

Notes: Bluer tones represent higher intensity and redder tones represent lower intensity for R-FTIR heat maps; the heat maps represent the boxed region in photo A.

Figure 11.

A) An R-FTIR area map of travertine (TRAV-WS3G) includes black-colored carbonate- and ferrous iron-rich regions (red star), white, transparent Si-O-rich regions (blue star), and red-colored carbonate- and ferrous iron-rich regions (yellow star). B) A frequency heat map of 1020 cm^{-1}, a wavenumber indicative of Si-O bonds, shows higher intensity in blue and green tones where that bond is in highest abundance. C, D and E) Spectra of representative black-colored carbonate- and ferrous iron-rich regions (red star), white, transparent Si-O-rich regions (blue star), and red-colored carbonate- and ferrous iron-rich regions (yellow star) are presented with a solid vertical line notating the location of the 976 cm^{-1} region and a dashed line notating the location of the 680 cm^{-1} region. Notes: Bluer tones represent higher intensity and redder tones represent lower intensity for R-FTIR heat maps; the heat map represents the boxed region in photo A.

Figure 12. A PCA of ATR-FTIR spectra of all samples separates the samples by lithologic types: ultramafics are located in the top right and carbonates in bottom right. Note: MAG-1 separated from rest by component 1 as a result of overall higher intensity of the spectrum compared to others.

Figure 13. A) A T-FTIR area map of serpentinite (SRP-1) includes serpentine-rich regions with veins and grains of magnetite spread throughout. B) A PCA heat map, conducted in OMNIC Atlµs based on the 2900 cm^{-1} (3000-2830 cm^{-1}) and 1600 cm^{-1} (1800-1500 cm^{-1}) peak areas, highlights regions of the first principle component (PC1) that have greater peak areas at the 2900 cm^{-1} and 1600 cm^{-1} wavenumber regions in red, yellow, and green tones. C) The value of PC1 indicates statistically significant presences of the 2900 cm^{-1} and 1600 cm^{-1} regions that correspond with mineralogically distinct regions. D) A heat map of an extracted line map (as indicated by the red vertical solid

line in photo A) shows an overall increase in intensity of the spectra where magnetite is abundant and a relative increase at the 2900 cm^{-1} and 1600 cm^{-1} regions.

Note: Redder tones represent are higher intensity and bluer tones are lower intensity for T-FTIR heat maps.

Figure 14. A) An R-FTIR line map was taken on a CROMO serpentinite (SRP-1) wafer incubated in the CROMO QV 1,1 well. Representative R-FTIR spectra before (B) and after (C) cleaning surface of the wafer with isopropyl alcohol are provided

Figure 15. ATR-FTIR of xanthan gum powder with peak assignments (Osiro et al. 2011) is shown.

Figure 16. A) An R-FTIR area map was taken at the boundary of a dried film of xanthan gum on SRP-1; points 1 and 8 overlay xanthan gum, point 15 overlies a thinner region of xanthan gum, and points 22 and 29 overlay serpentine without a xanthan gum film. B) A PCA comparing the full spectra of the marked sample points separates points 1, 8, and 15 (on xanthan gum film) from points 22 and 29 (off xanthan gum).

Figure 17. A) Spectra of xanthan gum experiment are shown with increasing xanthan gum concentration in serpentinite powder, in order from lowest (0 wt. % x.g.) to highest (100 wt. % x.g.). B) The same set of spectra are shown zoomed in to the 1600 cm^{-1} region. Peaks are labeled with potential bond assignments.

Figure 18. A) Peak height of the 1600 cm^{-1} region from 0 - 100 wt. % x.g. in powdered serpentinite matrix is presented. The best-fit line provides an R^2 of 0.9947. B) Peak height of the 1600 cm^{-1} region from 0 - 5 wt. % x.g in powdered serpentinite matrix is presented as a log function.

Figure 19. A) Peak area of the 1600 cm^{-1} region (1775-1500 cm^{-1}) from 0 - 100 wt. % x.g. in powdered serpentinite matrix is presented. The best-fit line provides an R^2 of 0.99405. B) Peak area of the 1600 cm^{-1} region (1775-1500 cm^{-1}) from 0 - 5 wt. % x.g in powdered serpentinite matrix is presented as a log function.

Figure 20. Peak location of the larger peak in the 1600 cm^{-1} region (1775-1500 cm^{-1}) from 0 - 100 wt. % x.g. in powdered serpentinite matrix is presented. The best-fit logarithmic curve provides an R^2 of 0.79656. B) Peak location of the larger peak in the 1600 cm^{-1} region (1775-1500 cm^{-1}) from 0 - 5 wt. % x.g in powdered serpentinite matrix is presented as a log function.

APPENDIX

Appendix Table 1. Xanthan gum and ground serpentinite proportions made in lab for xanthan gum experiment range from 0 - 100 wt% x.g.

Total mass (g)	Mass of serpentinite (g)	Mass of x.g. (g)	Concentration of x.g. (wt. %)
10.0000	9.9999	0.0001	0.001
10.0000	9.9990	0.0010	0.010
1.0000	0.9990	0.0010	0.10
1.0000	0.9900	0.0100	1.00
1.0000	0.9800	0.0200	2.00
1.0000	0.9500	0.0500	5.00
1.0000	0.8000	0.2000	20.00
1.0000	0.5000	0.5000	50.00
1.0000	0.2000	0.8000	80.00
1.0000	0.0000	1.0000	100.00
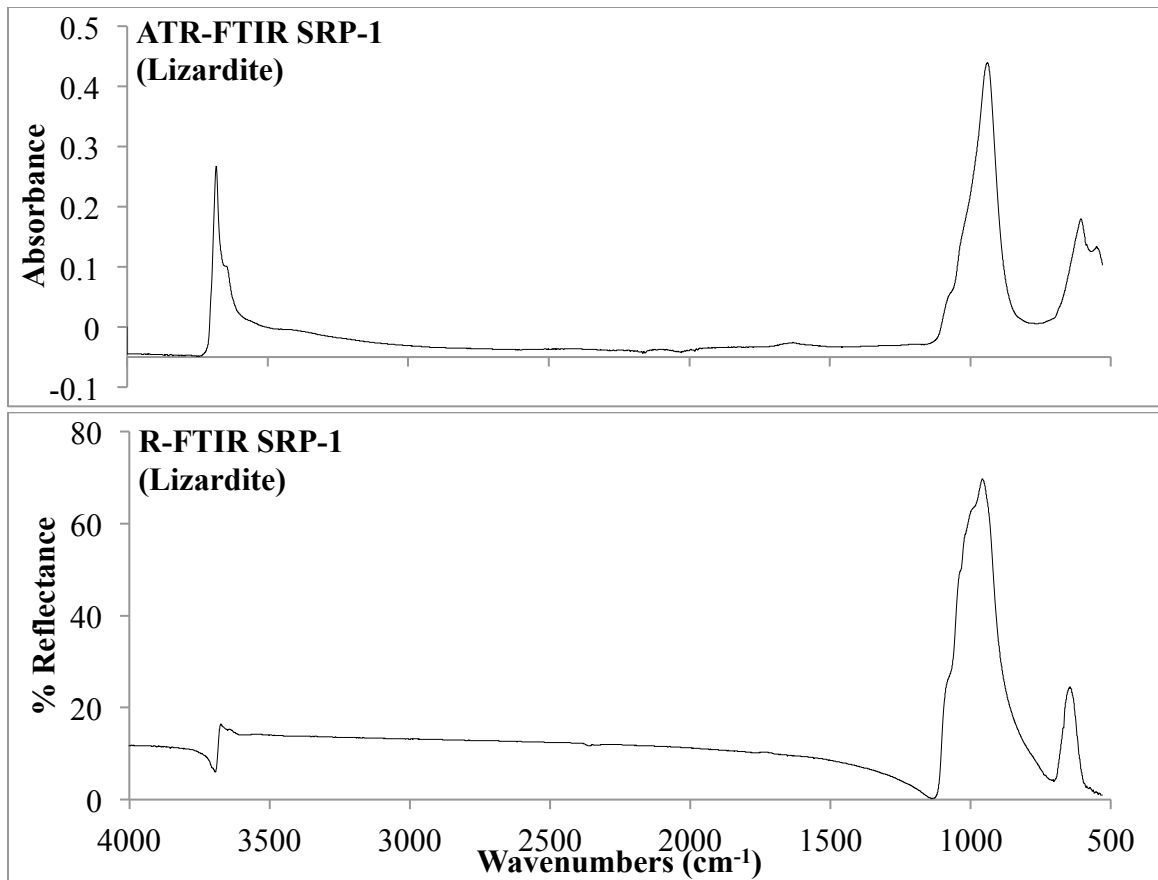
Appendix Figure 1. ATR-FTIR and R-FTIR spectra of serpentinite from Coast Range

Ophiolite (SRP-1).
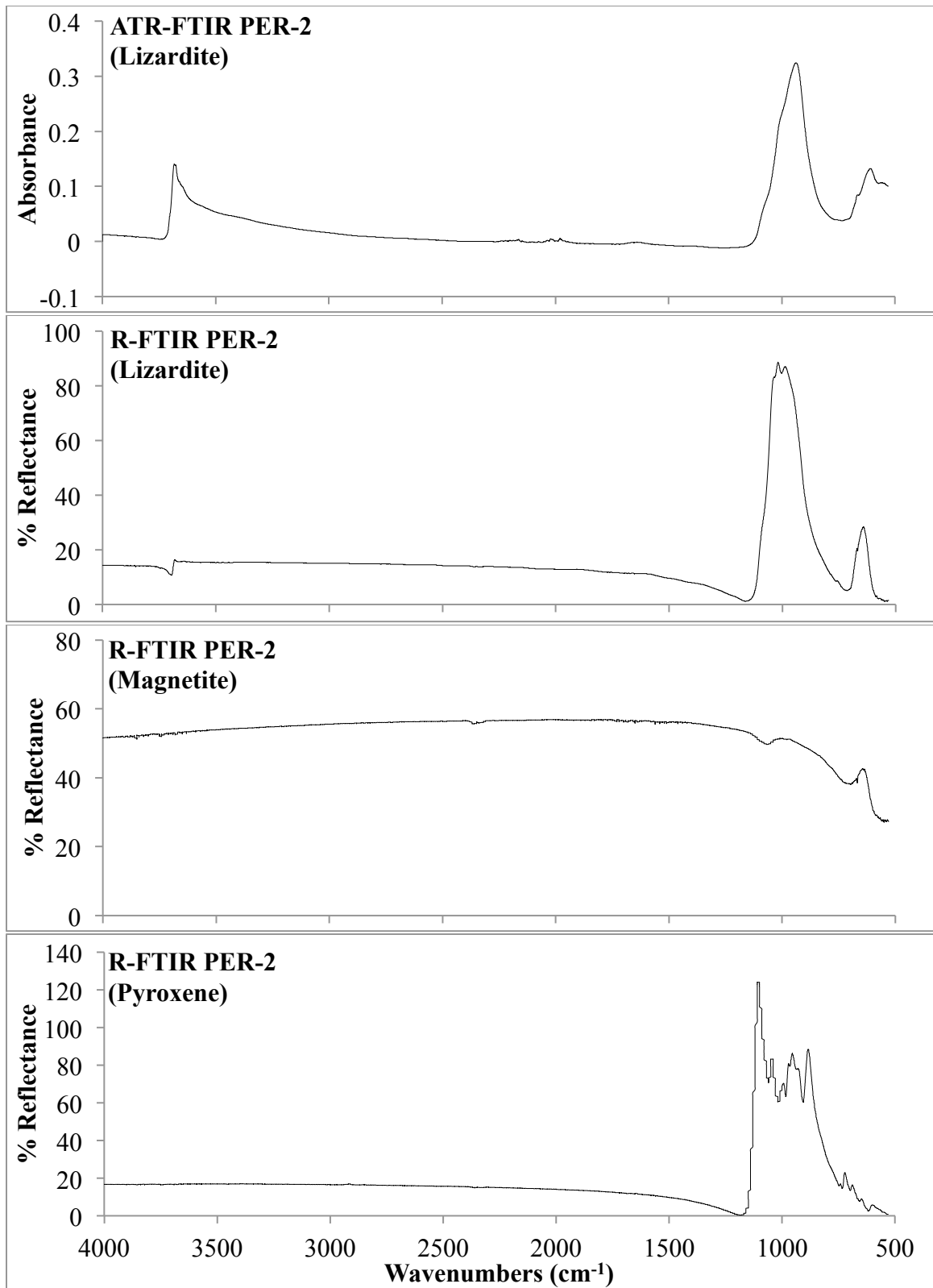
Appendix Figure 2. ATR-FTIR and R-FTIR spectra of peridotite from Yellow Dog, MI

(PER-2).
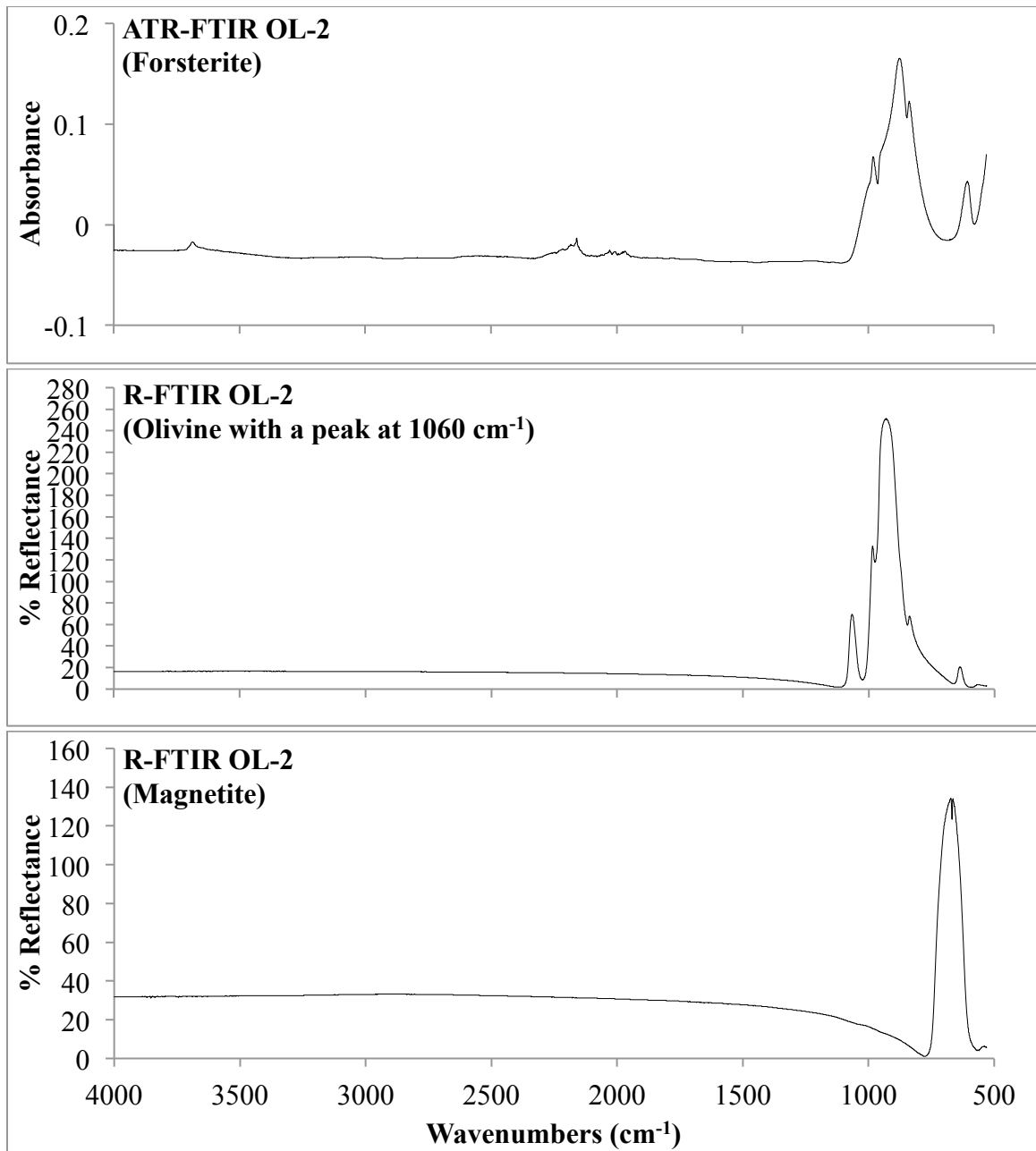
Appendix Figure 3. ATR-FTIR and R-FTIR spectra of olivine from Twin Sister's Range, WA (OL-2).
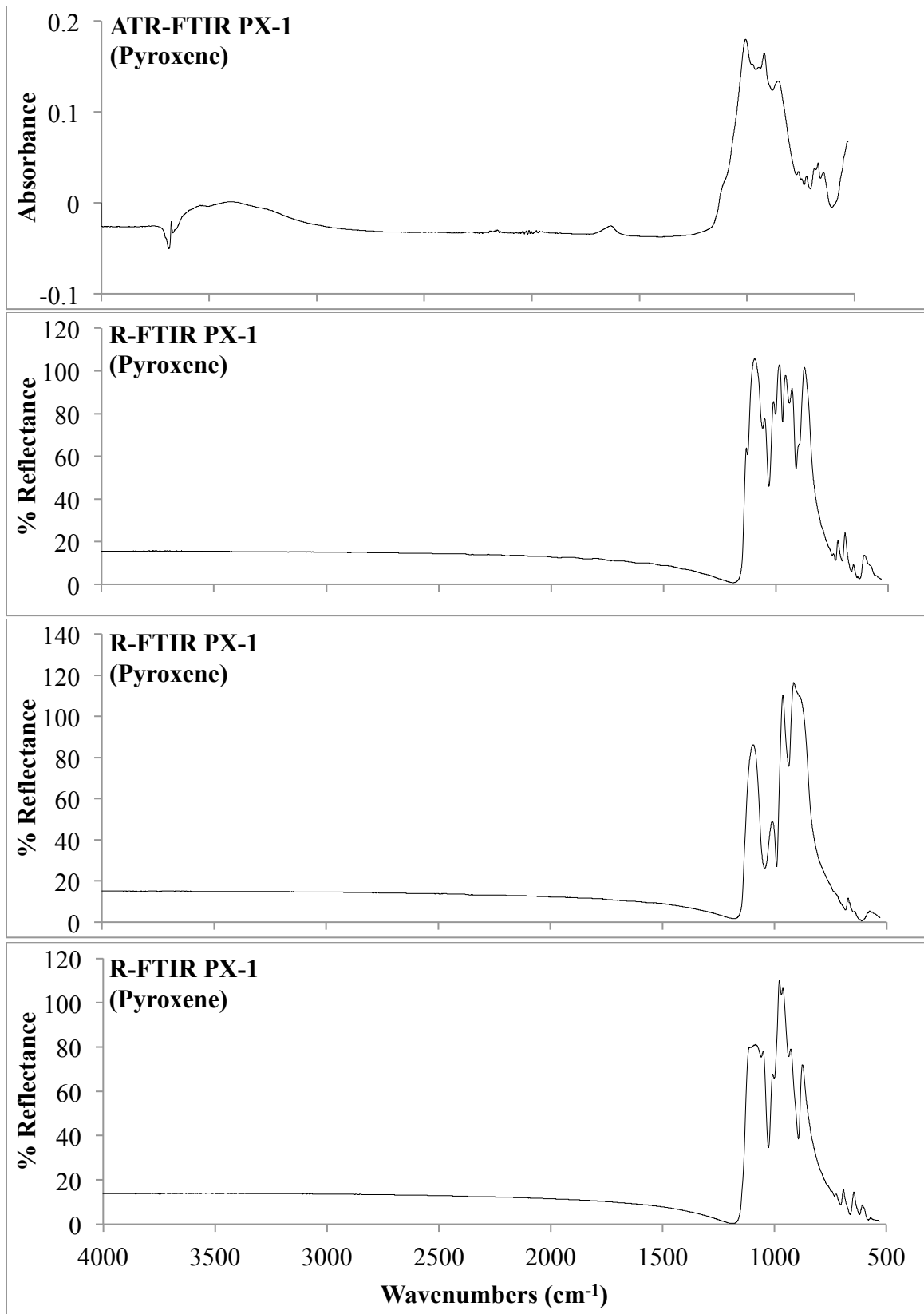
Appendix Figure 4. ATR-FTIR and R-FTIR spectra of dunite from Taskesti, Turkey (PX-1).
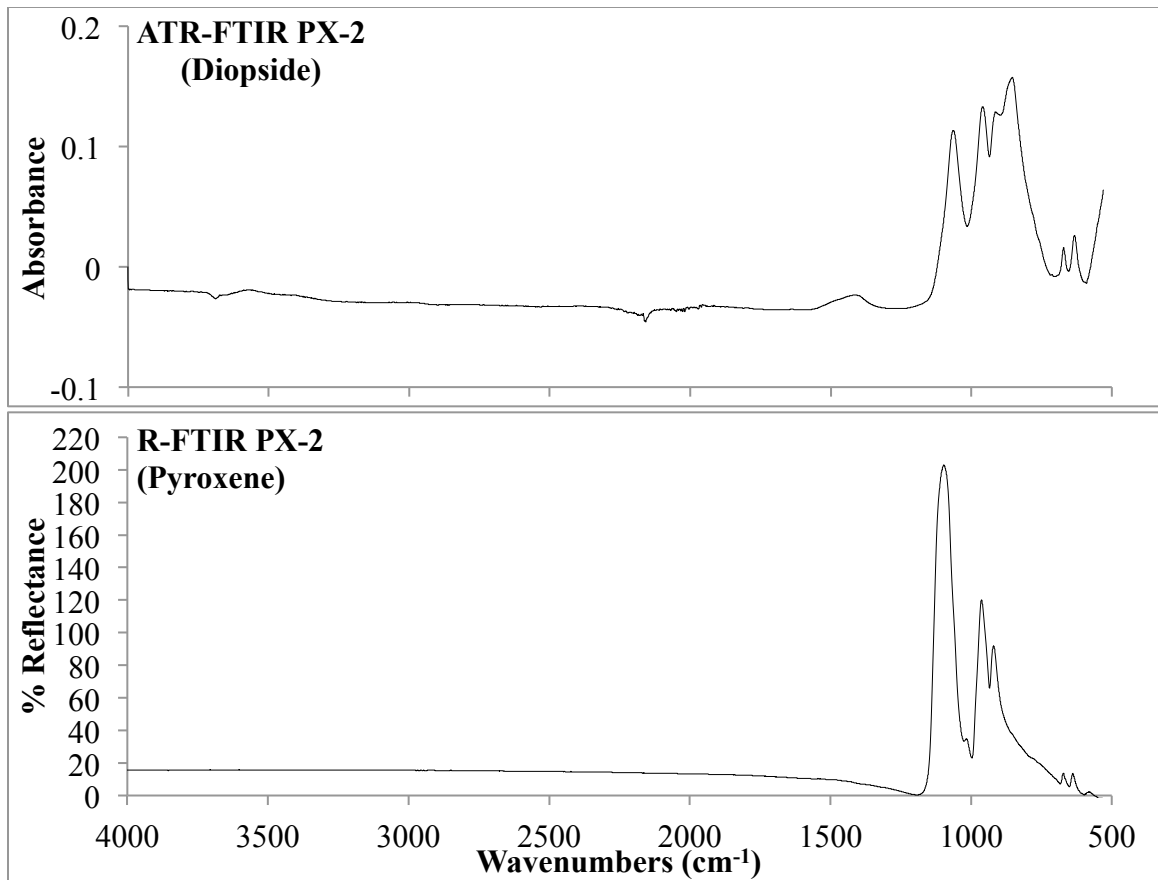
Appendix Figure 5. ATR-FTIR and R-FTIR spectra of diopside from ON, Canada (PX-

2).
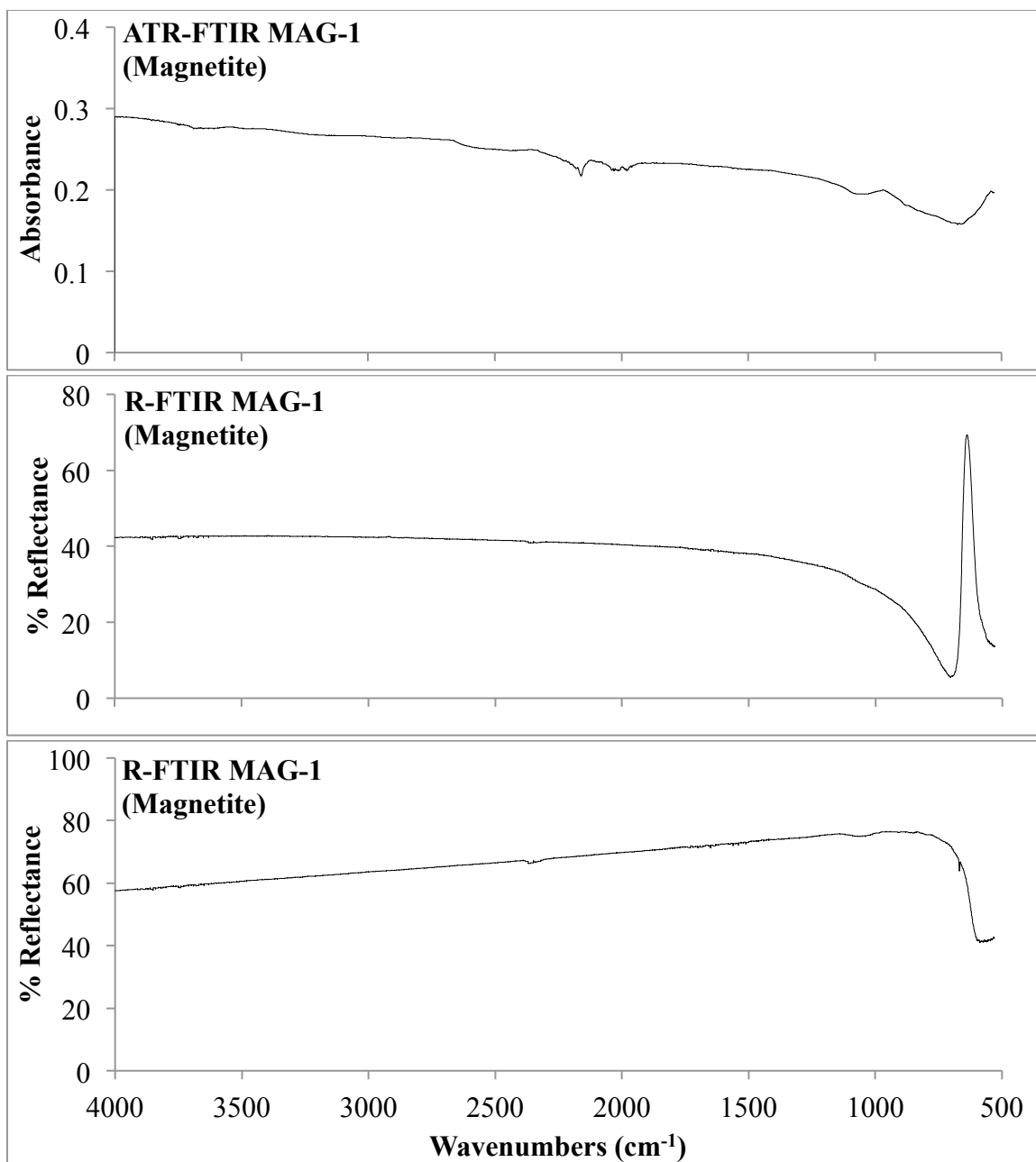
Appendix Figure 6. ATR-FTIR and R-FTIR spectra of magnetite from Ishpeming, MI

(MAG-1).
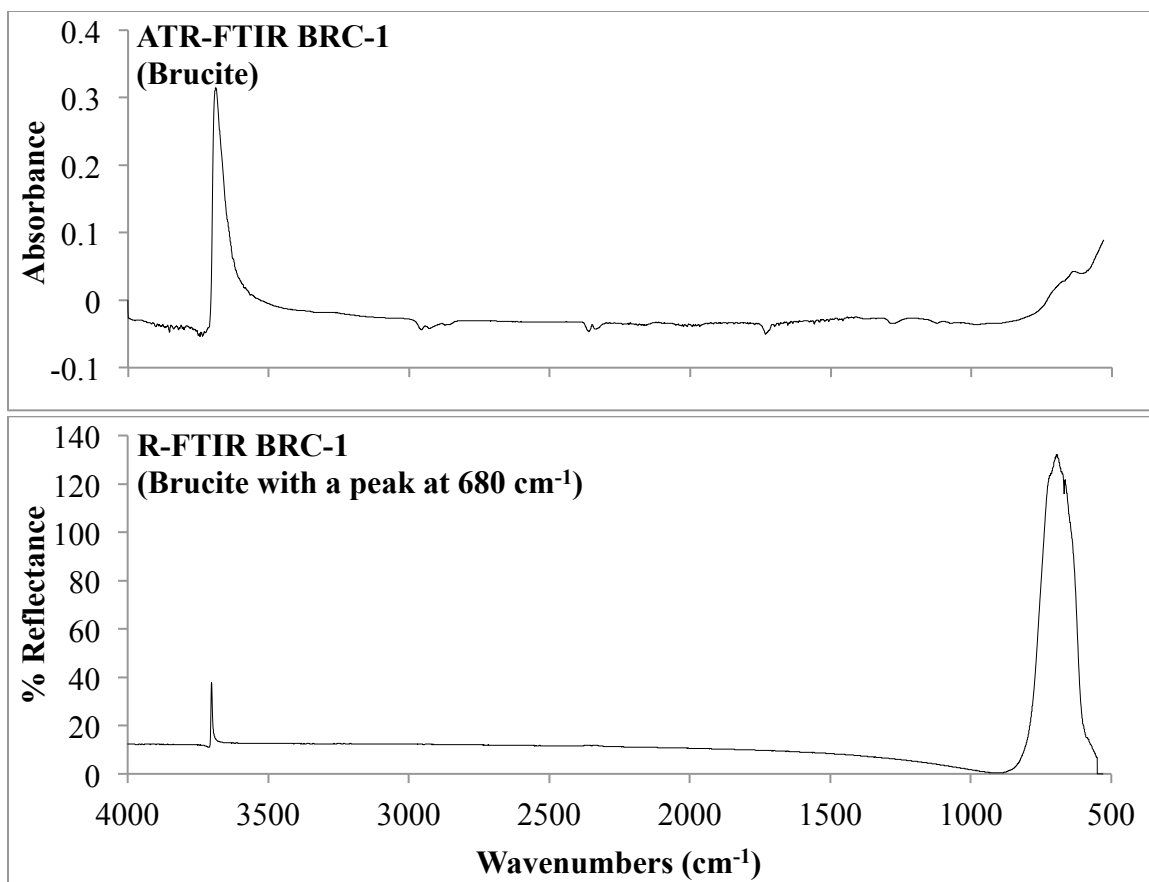
Appendix Figure 7. ATR-FTIR and R-FTIR spectra of brucite from Belkis Minerals in

AZ (BRC-1).
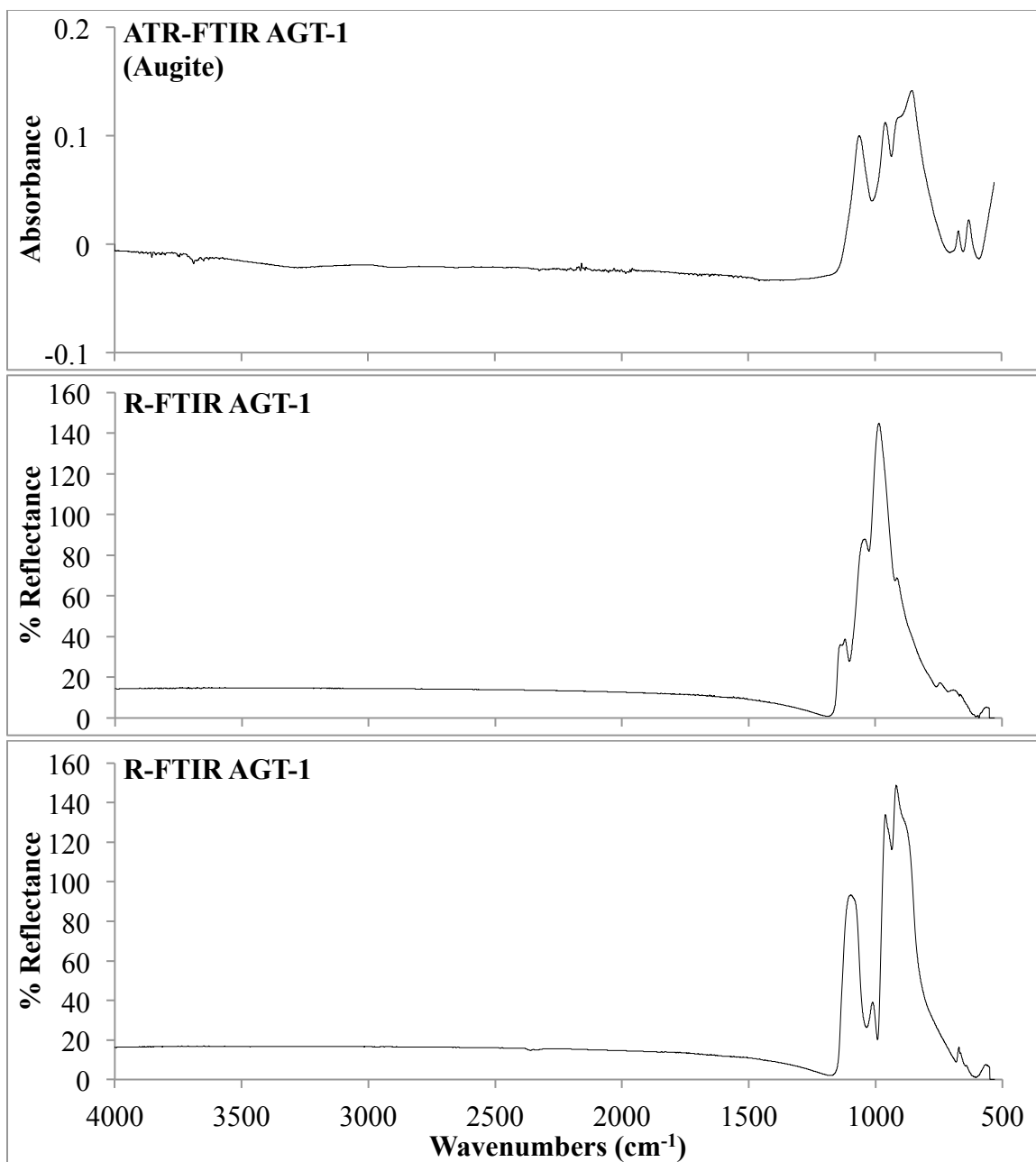
Appendix Figure 8. ATR-FTIR and R-FTIR spectra of Augite (AGT-1).
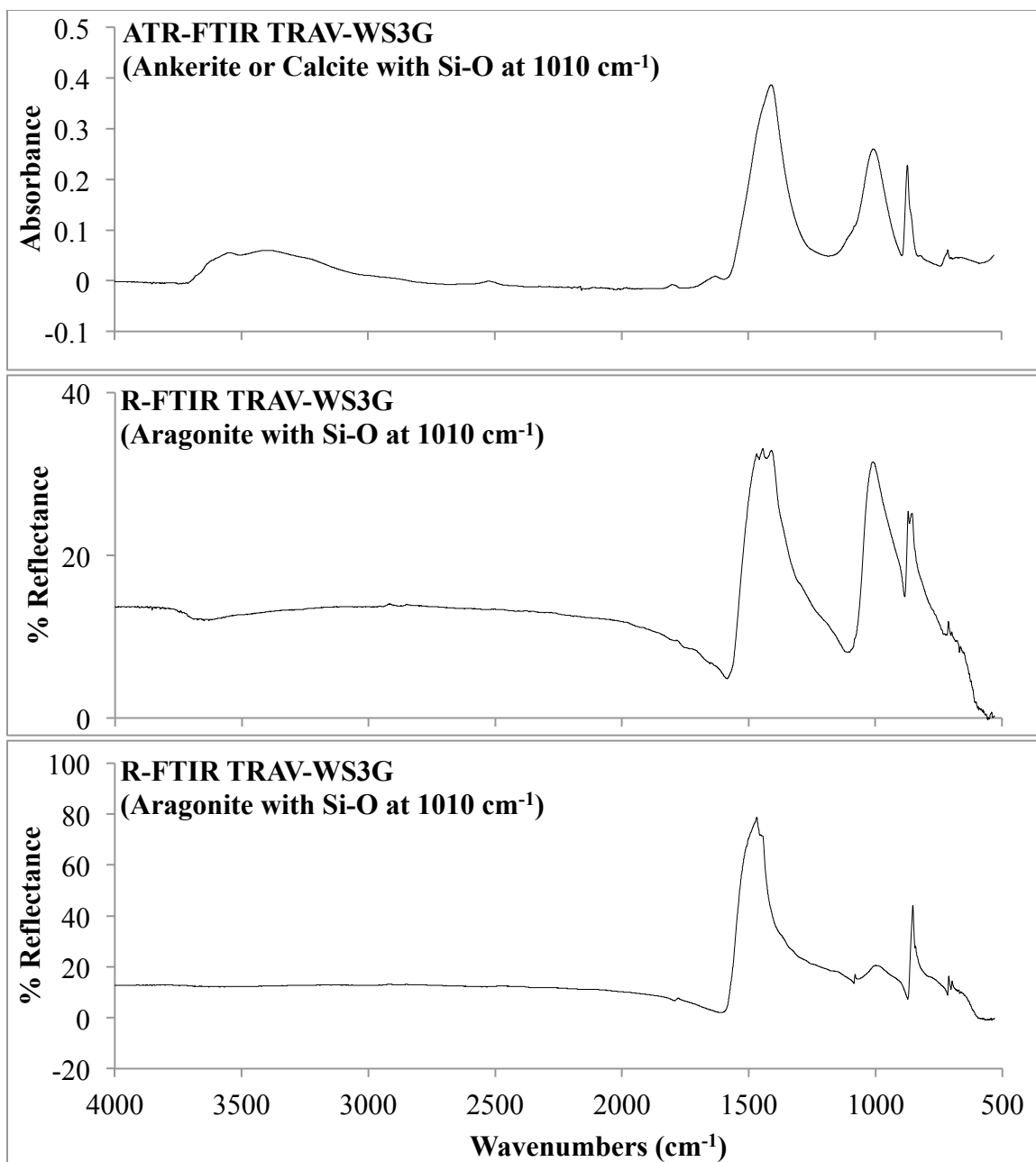
Appendix Figure 9. ATR-FTIR and R-FTIR spectra of Travertine from CROMO (TRAV-WS3G).
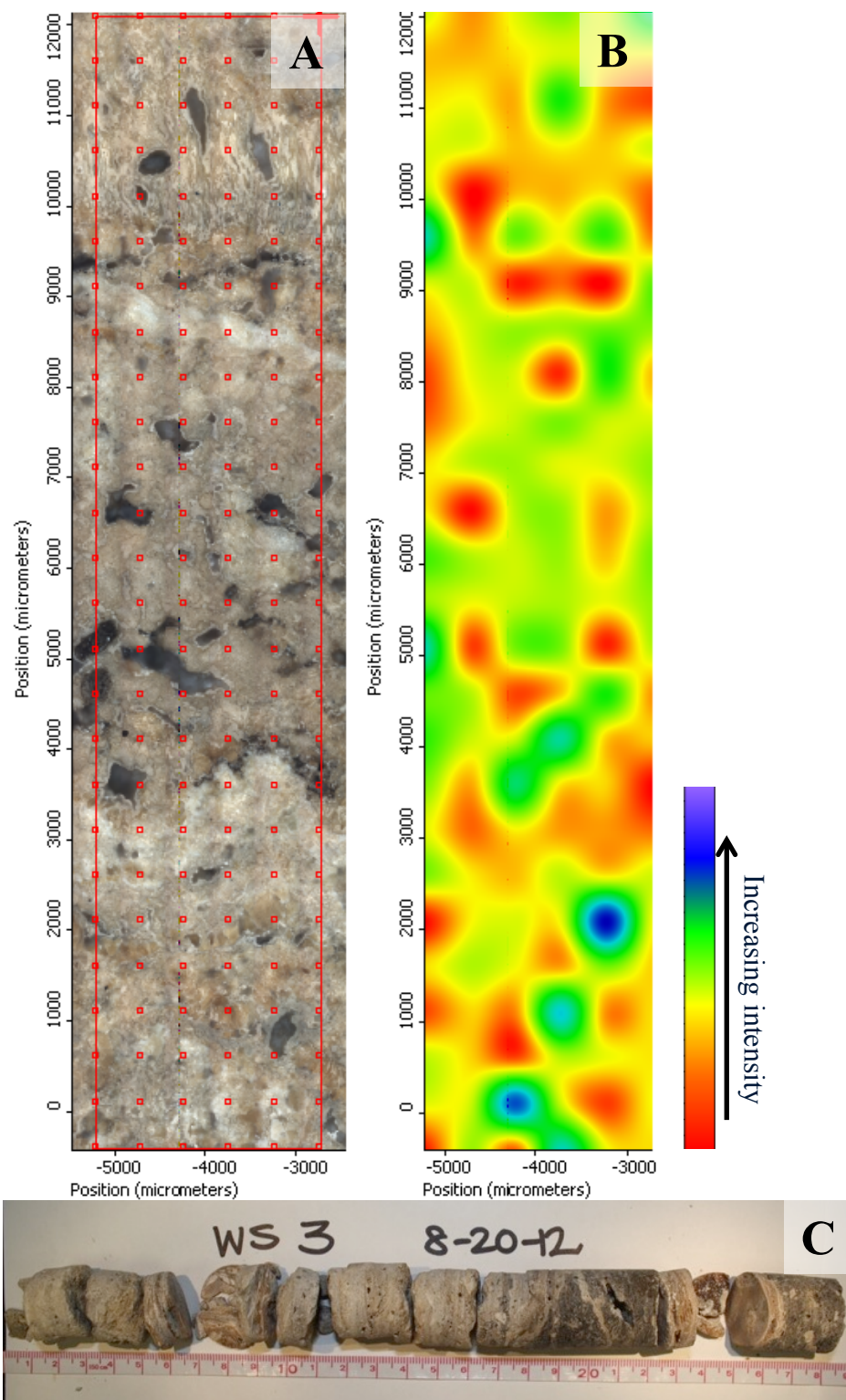
Appendix Figure 10. A) Sample points of an area map are plotted on polished TRAV-WS3G. B) R-FTIR frequency heat map of 1006 cm^{-1}(Si-O) from the same area map. C) Travertine mini-core "WS 3" in 10C. Note cm scale along horizontal edge of image.

Prominent features can be observed at 7-9 cm and 20 cm. Darker phases (clay rich and/or containing serpentinite fragments) occur at 18-23 cm and ~27 cm.
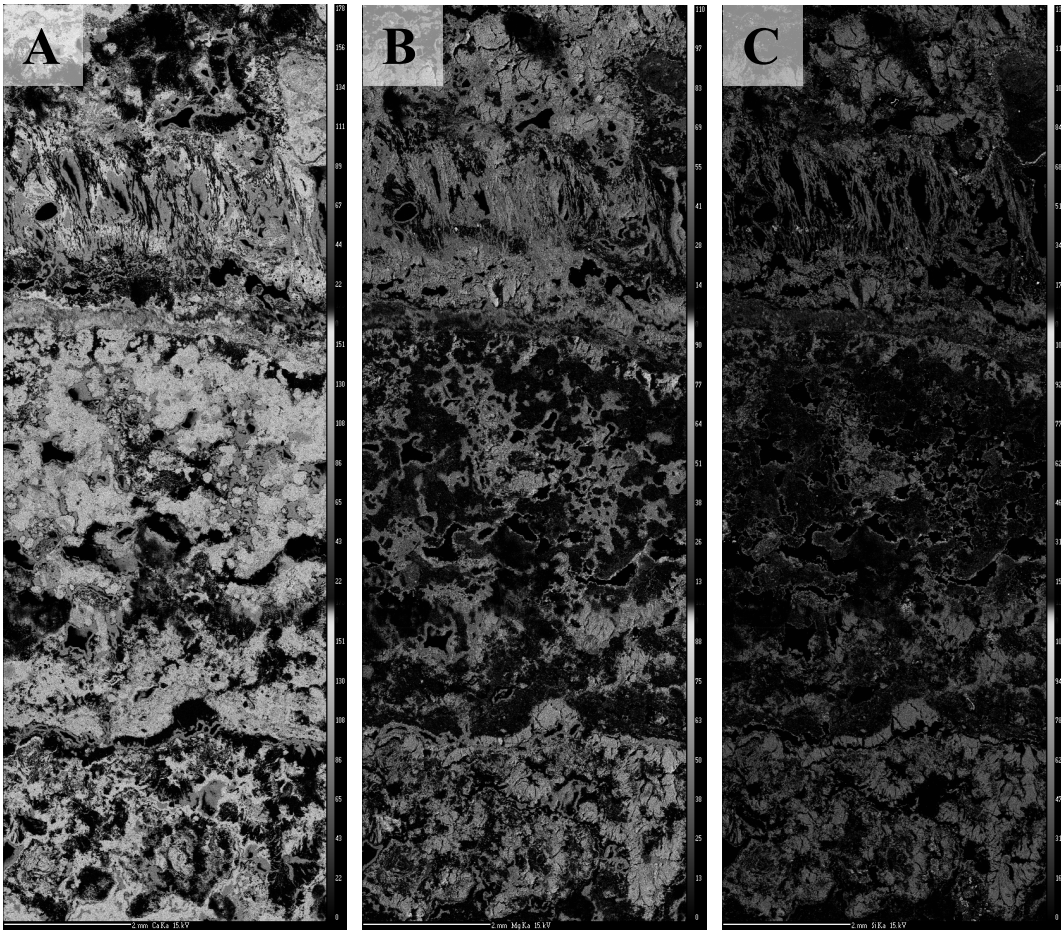
Appendix Figure 11. Microprobe element maps (A) calcium, B) magnesium, and C) silicon) of an intact section of the CROMO travertine mini-core TRAV-WS3G was collected on the microprobe at Brown University. We observe the interwoven texture of Si (in lower concentration) and Mg around Ca. Note: lighter grey represents high concentration, darker is low.

	White Seep 3_C	White Seep 3_D	White Seep 3 _F
Top	Image 0	Image 100	Image 100
Top-Middle	Image 50	Image 250	Image 425
Middle	Image 100	Image 400	Image 750
Middle-Bottom	Image 150	Image 550	Image 1075
Bottom	Image 200	Image 700	Image 1400
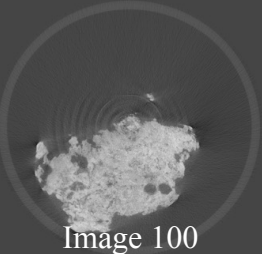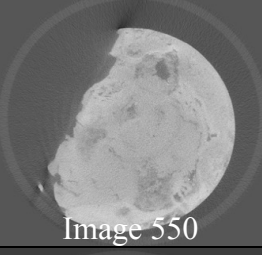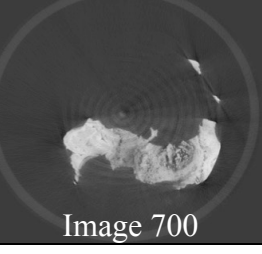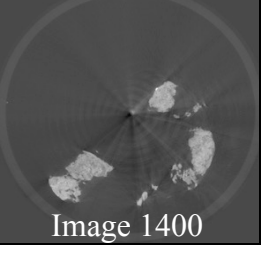
Appendix Figure 12. µCT scans of a travertine mini-core from the White Seep (WS) at CROMO (obtained with a hand-held ASC Scientific Electric Core Drill Model DE-T3) were collected in 15-µm-thick slices by a SCANCO Medical µCT 40 scanning unit at the McCulloch µCT imaging facility at Rhode Island Hospital. Included here are

representative slices from top to bottom of sections C, D, and F, which denote mini-core

intact sections, with A as the near-surface section. Section C (left column) is from ~5-6

cm, Section D (mid) is from ~7-9.5 cm, and Section F (right) is from ~11.5-14 cm in the

photo provided in Appendix Figure 10C. Variable density with depth is observed, due to

shifting carbonate mineralogy/intercalated clay minerals/encapsulated fragments of

country rock. Note: dark areas are less dense than light areas.

Table 1

Sample ID	Lithology	Location	XRD Mineral ID
Ultramafics			
SRP-1	Serpentinite	CROMO's quarry valley surface serpentinite	Lizardite, Antigorite, Magnetite
SRP-2	Serpentinite	Poon Bato, Philippines	Lizardite, Antigorite, Magnetite, Clinopyroxene, Smectite
SRP-3	Serpentinite	Jade Mtn Lodge, Crescent City, CA	Lizardite, Antigorite, Magnetite, Calcite
PER-1	Peridotite	Lake Ronald, New Zealand	Forsterite, Enstatite
PER-2	Peridotite	Yellow Dog, MI	Hedenburgite, Enstatite, Forsterite, Lizardite, Antigorite, Magnetite
OL-1	Olivine	Fisher Scientific	Forsterite, Antigorite, Magnetite
OL-2	Olivine	Twin Sisters Range, WA	Forsterite, Antigorite, Magnetite
PX-1	Pyroxenite	Taskesti, Turkey	Pyroxene, Smectite
PX-2	Diopside	Bird CK, Herschel, ON, Canada	Diopside, Hedenbergite, Tremolite
MAG-1	Magnetite	Ishpeming MI	Magnetite, Columbite
BRC-1	Brucite	Arizona	Brucite
AGT-1	Augite		
Carbonates			
TRAV-WS3G	Travertine	CROMO white seep	Carbonates (Ankerite, Calcite, Dolomite, Kutnohorite, Magnesite, Siderite), Lizardite, Smectite
DOL-1	Dolomite	Sussex County, NJ	Dolomite , Magnetite
CAL-1	Optical Calcite	Iceland	Calcite

Table 2.

Mineral	Peak Frequency	Peak Height	Peak Shape
Serpentine			
Antigorite	3670	Medium	Sharp
	980	Strongest	Sharp with short shoulder at 1047
	609	Strong	Sharp with slight shoulder at 603 and blended shoulders at 690 and 780 (broad)
	545	Strong	Sharp
Lizardite	3680	Strong	Sharp
	930	Strongest	Sharp with blended shoulder at base at 1050
	601	Medium	Sharp with a shoulder at 534
Pyroxene			
Augite	1060	Medium	
	854	Strongest	Sharp with sharp shoulder at 916
	640	Weakest	Sharp
	625	Weak	Sharp
Diopside	1060	Strong	Sharp
	956	Strong	Sharp
	852	Strongest	Sharp with blended shoulder at base at 894
	640	Weakest	Sharp
	630	Weak	Sharp
Enstatite	919	Strongest	Medium with shoulders at 1030, 983, 917, and 863
	709	Weakest	Sharp
	701	Very weak	Sharp
	680	Weak	Sharp
	646	Weak	Sharp
	640	Weak	Sharp
Hedenbergite	1045	Strong	Sharp
	950	Strong	Sharp
	850	Strongest	Sharp with blended shoulder at 894
	665	Weakest	Sharp
	620	Weak	Sharp
Olivine			
Fayalite	858	Strongest	Sharp with sharp, strong shoulders at 906 and 823
Forsterite	875	Strongest	Sharp with sharp, medium shoulders at 931 and 835
	601	Medium	Sharp

Carbonate			
Ankerite	1401	Strongest	Sharp with broad base
	867	Medium	Sharp
	723	Weak	Sharp
Aragonite	1440	Strongest	Sharp with broad base
	1083	Weak	Sharp
	854	Medium	Sharp
	711	Weak	Sharp
	700	Weakest	Sharp
Calcite	1390	Strongest	Sharp with broad base
	871	Medium	Sharp
	711	Weak	Sharp
Dolomite	1417	Strongest	Sharp with broad base
	875	Medium	Sharp
	728	Weak	Sharp
Magnesite	1428	Strongest	Sharp with broad base
	877	Medium	Sharp
	748	Weak	Sharp
Siderite	1400	Strongest	Sharp with broad base
	862	Medium	Sharp
	738	Weak	Sharp
Related Minerals			
Brucite	3689	Strongest	Sharp
	1400	Weakest	Broad
	592	Weak	Broad shoulder to a peak below frequencies of interest
Clinochlore	3540	Medium	Medium
	3578	Medium	Medium
	1411	Weak	Medium
	952	Strongest	Sharp with weak sharp shoulder at 830
	642	Strong	Sharp with broad blended shoulder at 701
Magnetite	All	Strong	One broad peak
Nontronite	3780	Strong	Broad
	3564	Strong	Sharp
Spinel	655	Strongest	Sharp
	555	Weak	Shoulder to a peak below frequencies of interest
Talc	3675	Weak	Sharp and very narrow
	995	Strongest	Sharp
	663	Medium	Sharp with broad blended shoulder at 750 and 690, and 636, and a sharp shoulder at 595

FIGURES
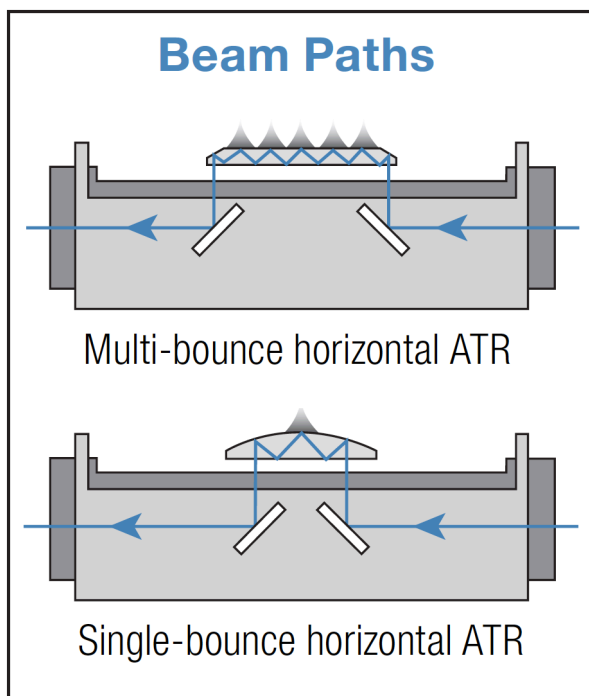
Figure 1
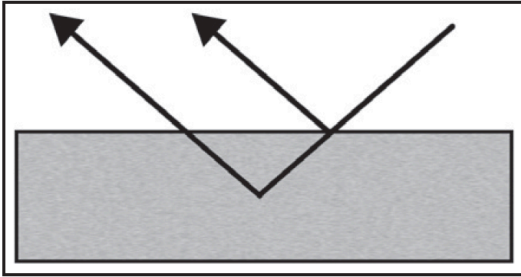
Diagram of the interaction of the
beam using true specular reflectance
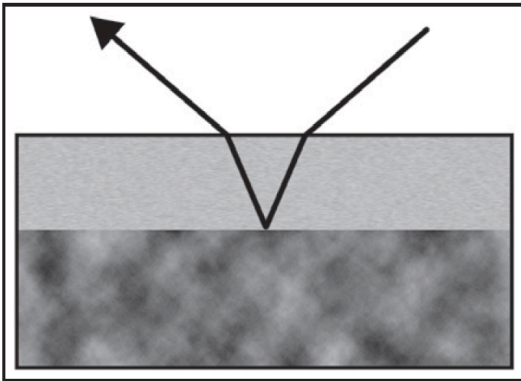
Diagram of the interaction of the
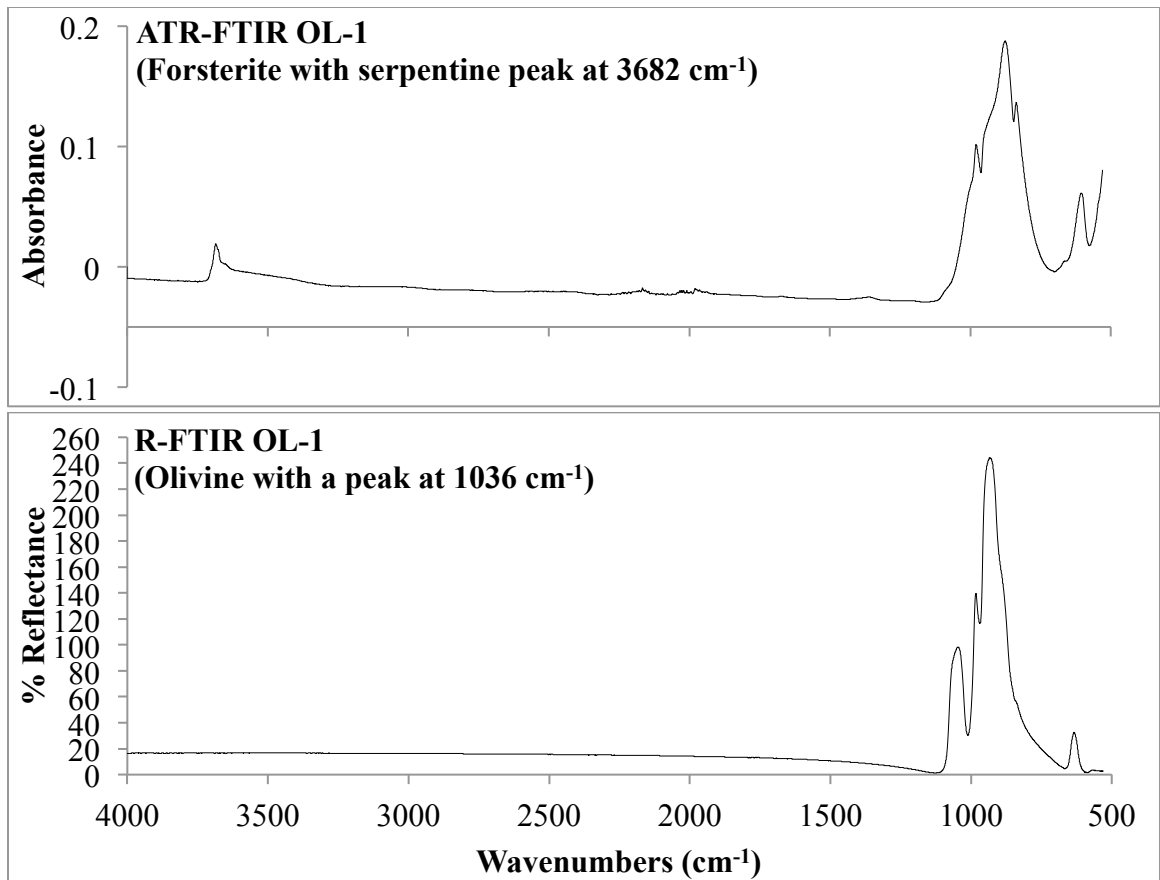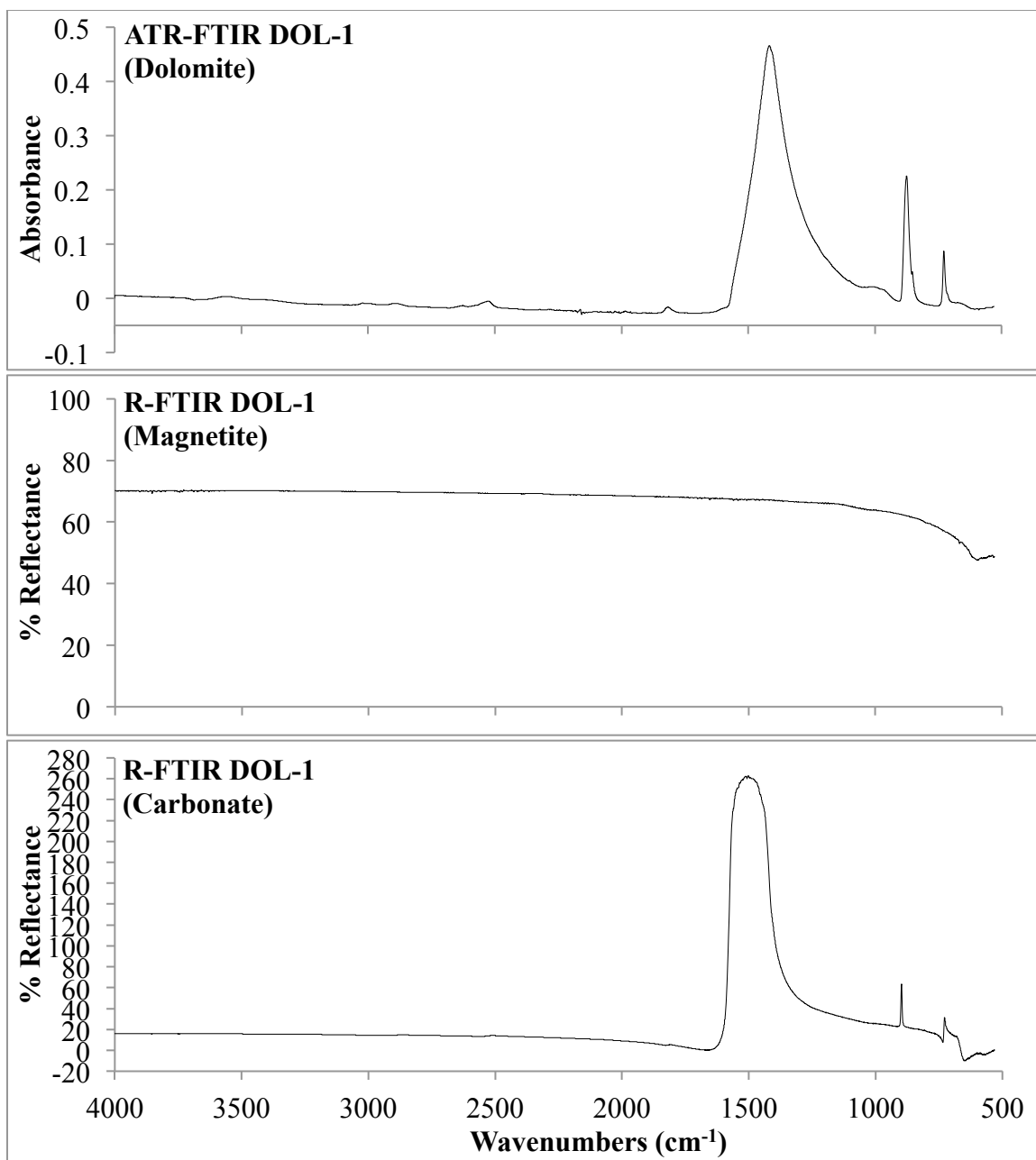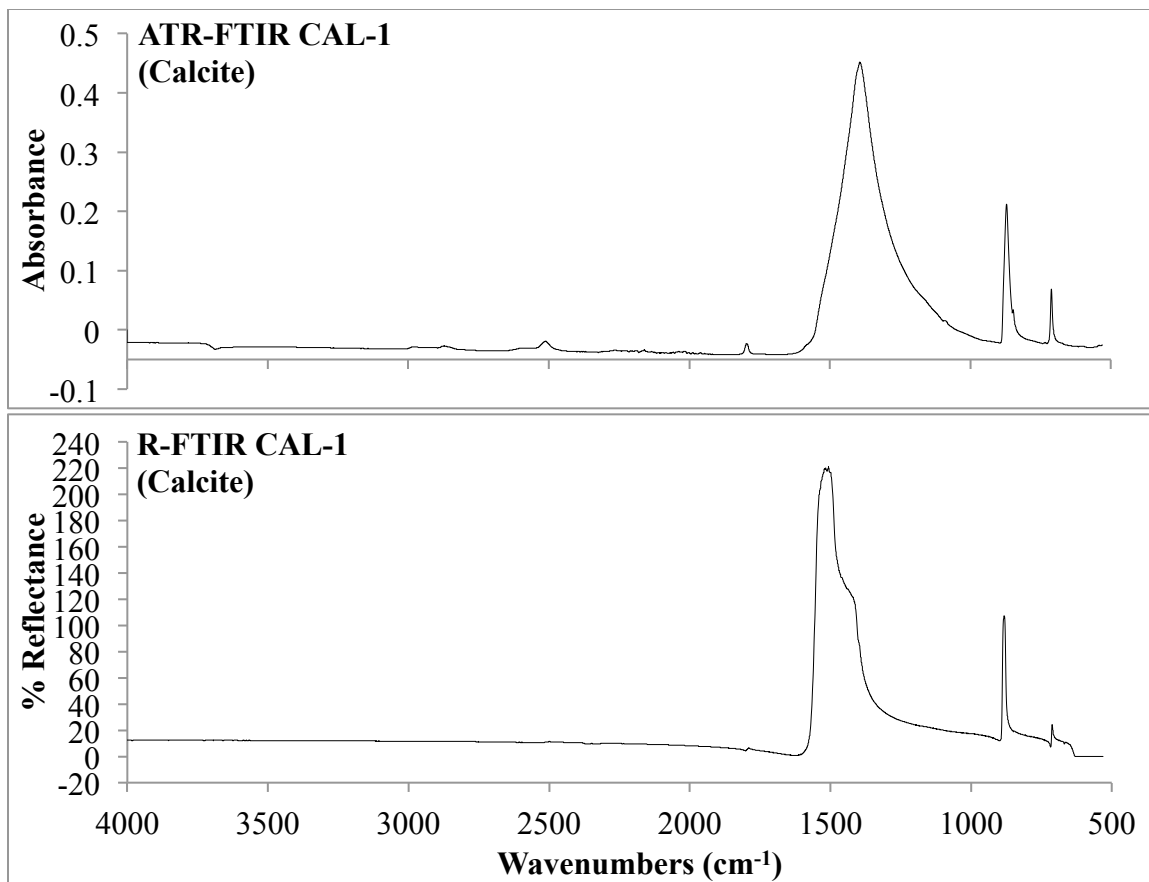beam using reflection-absorption
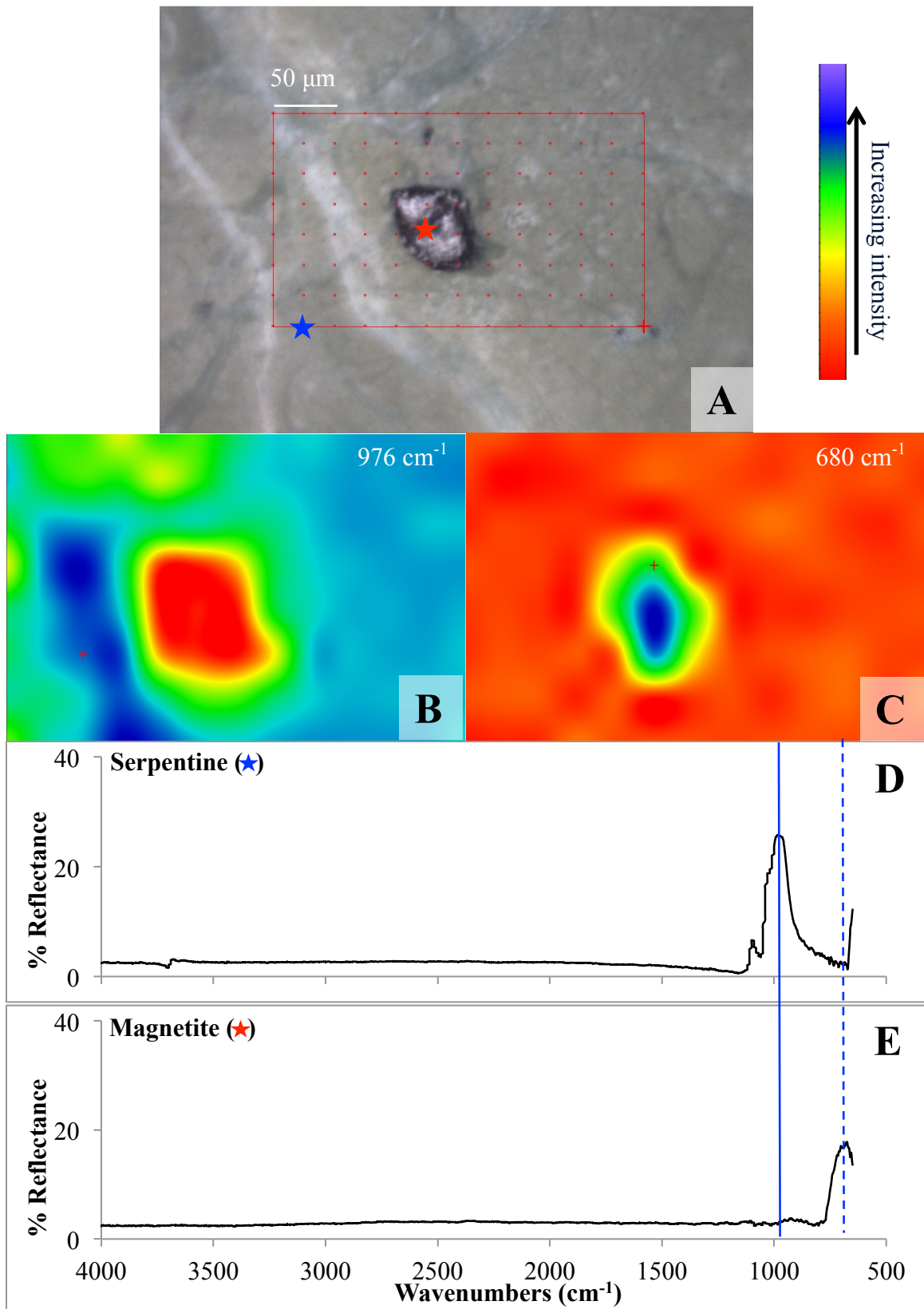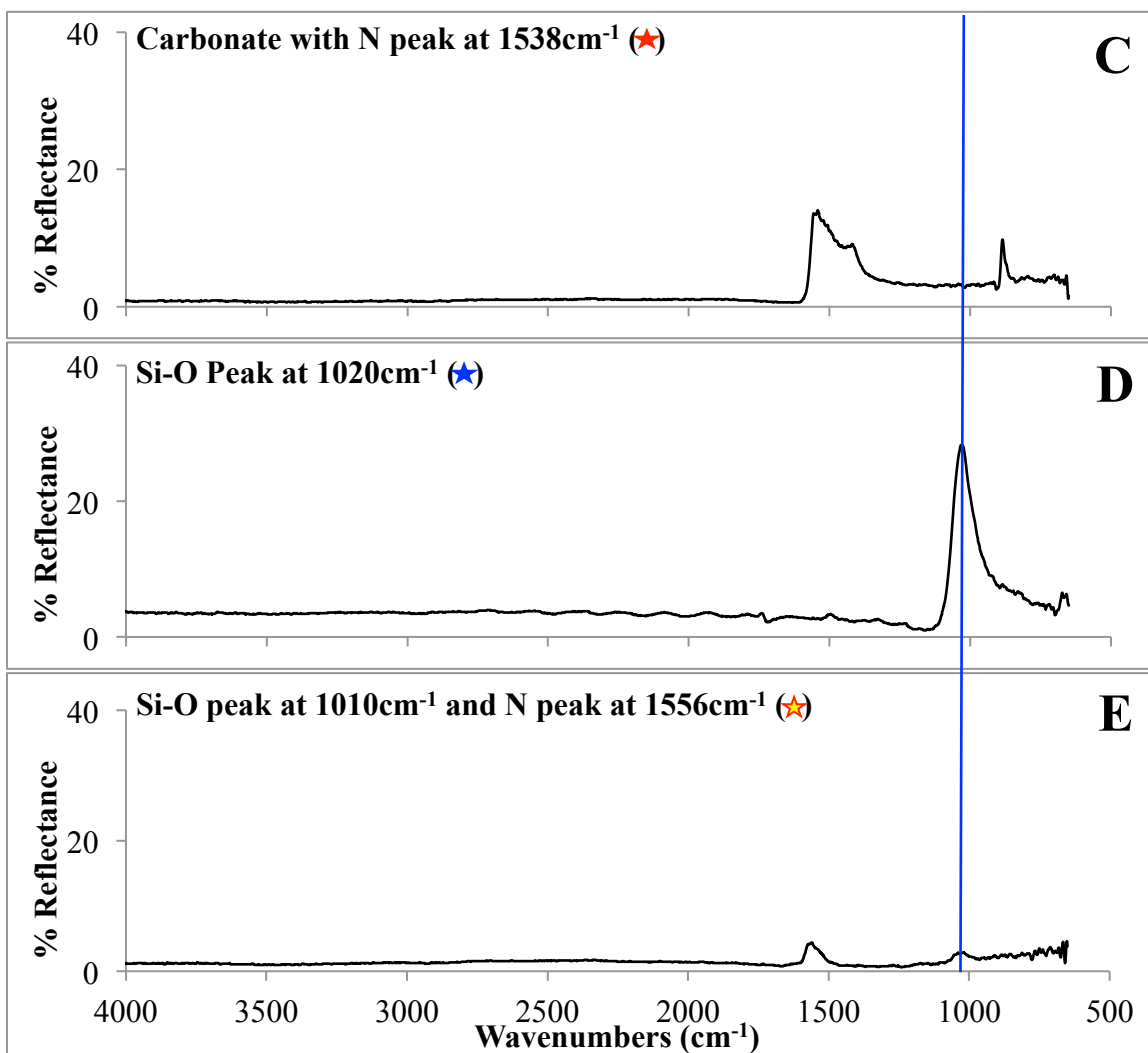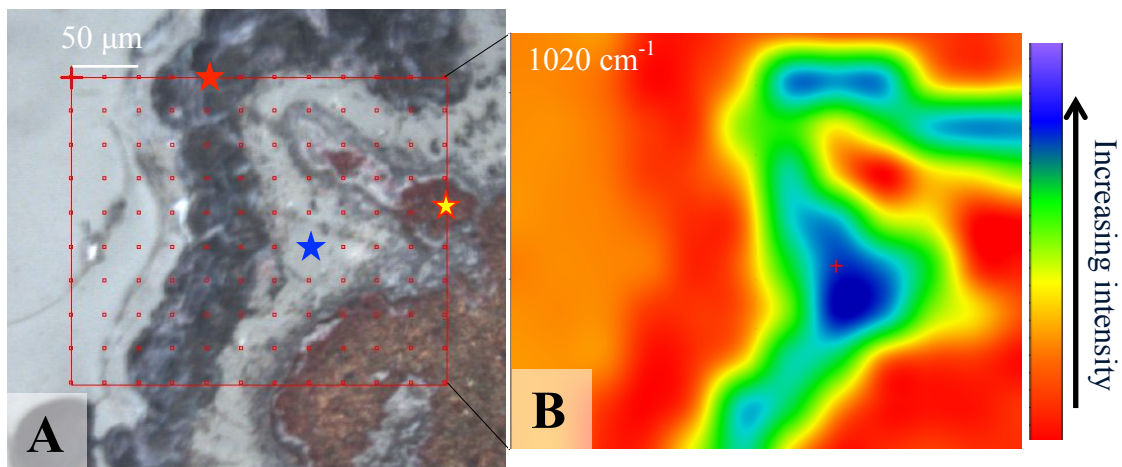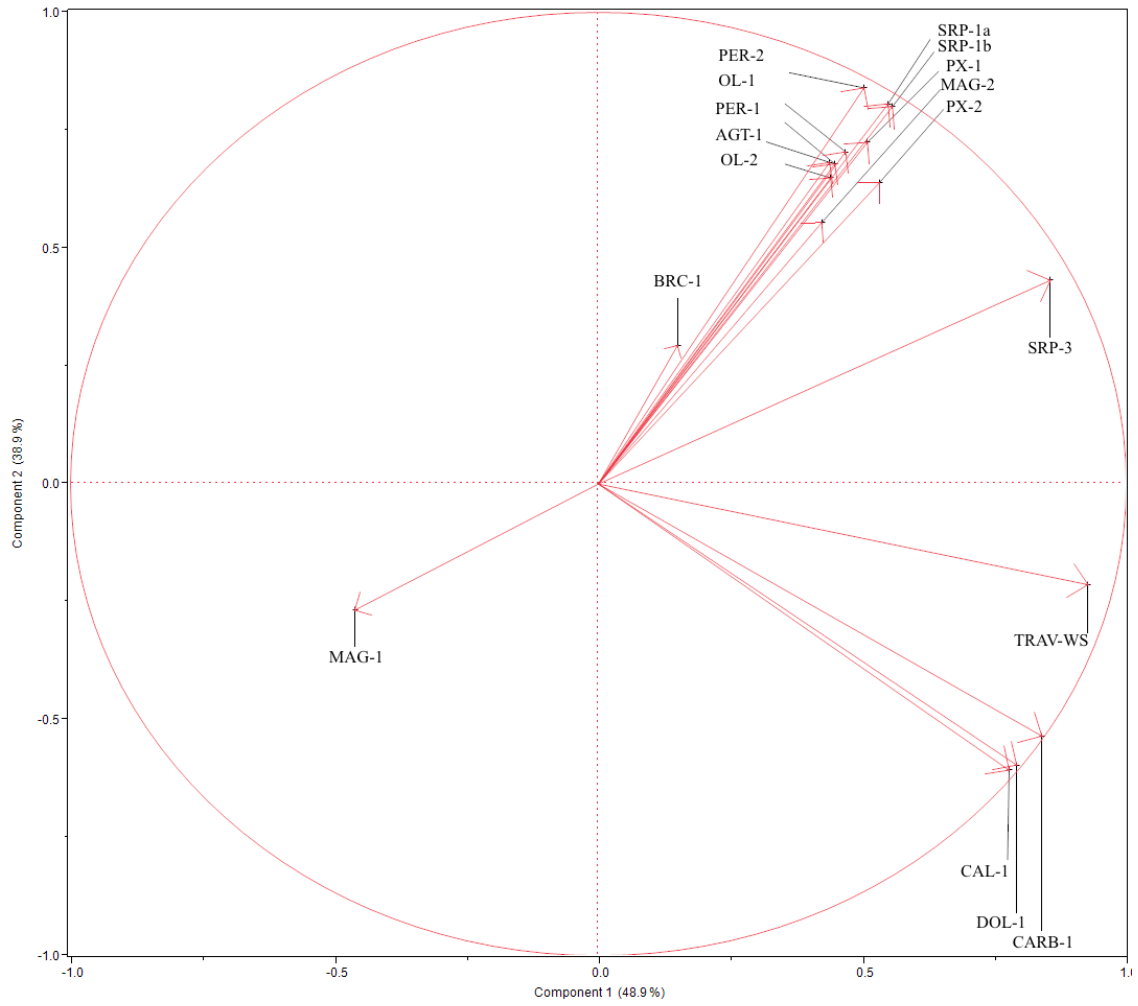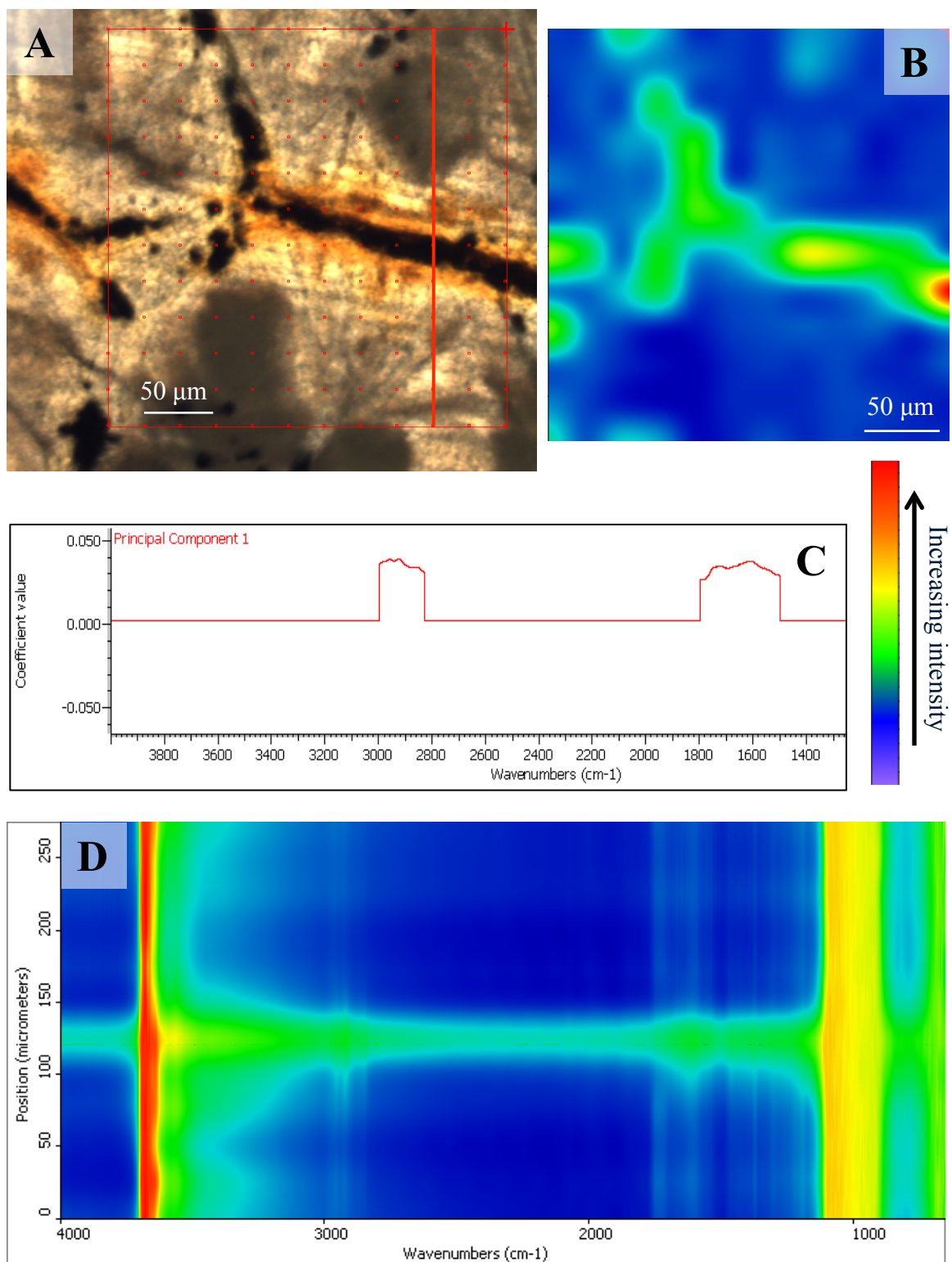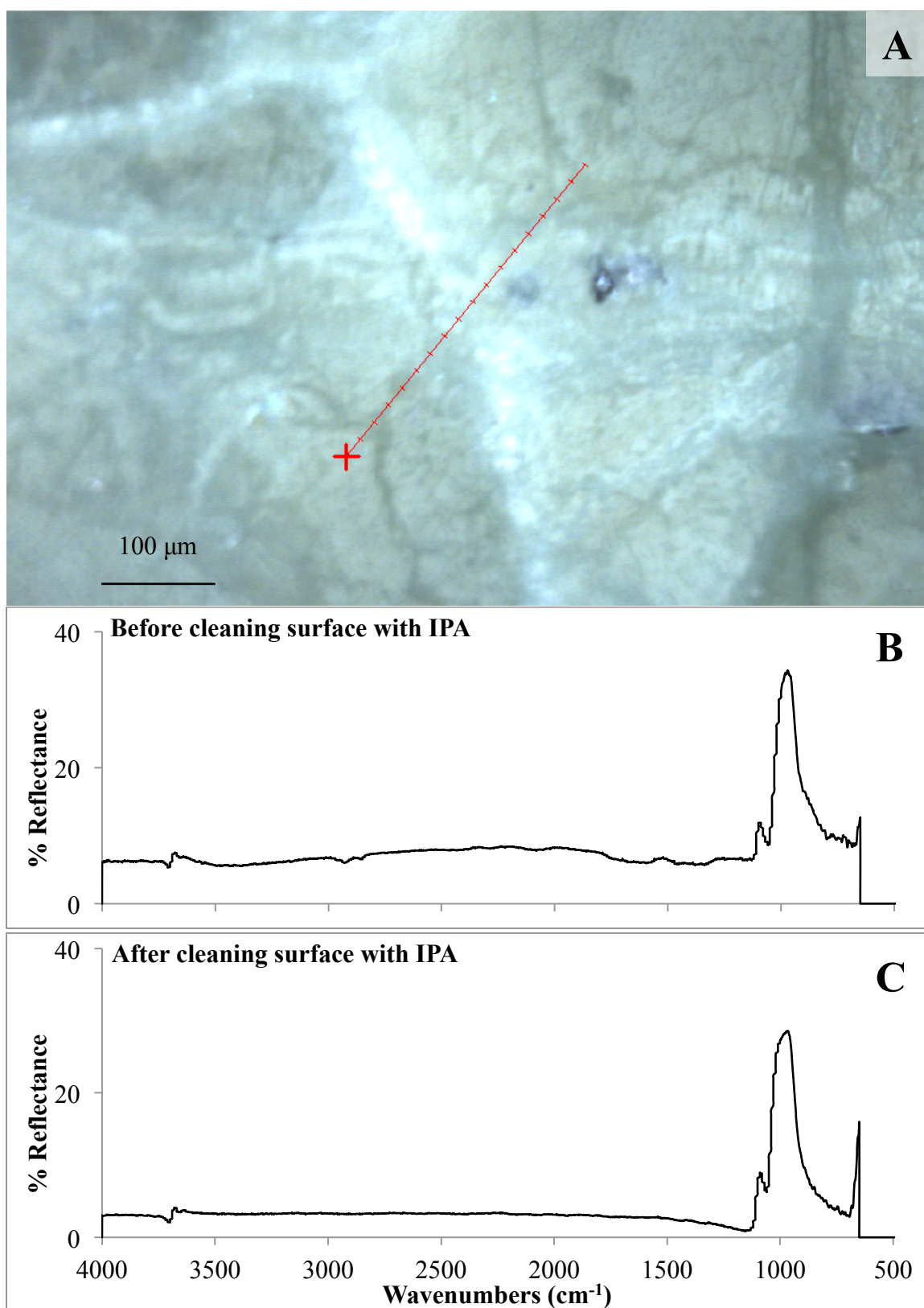
Figure 2

Figure 3

Figure 4

50
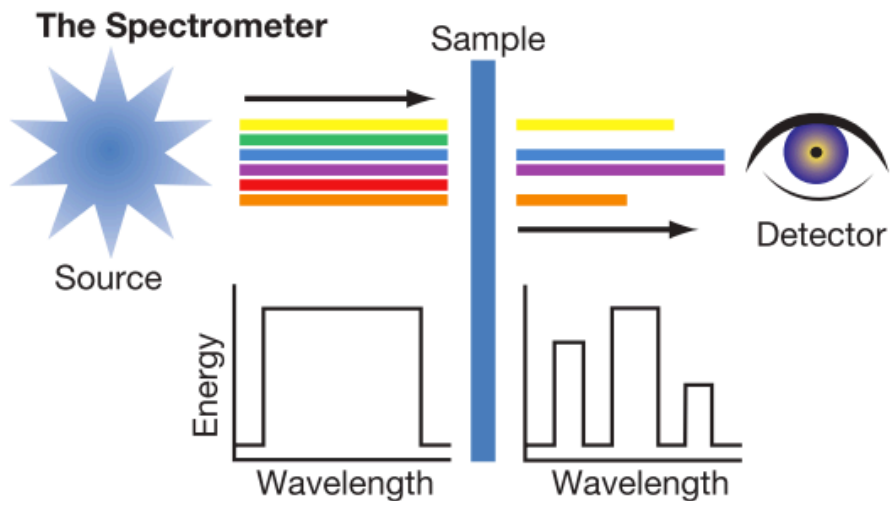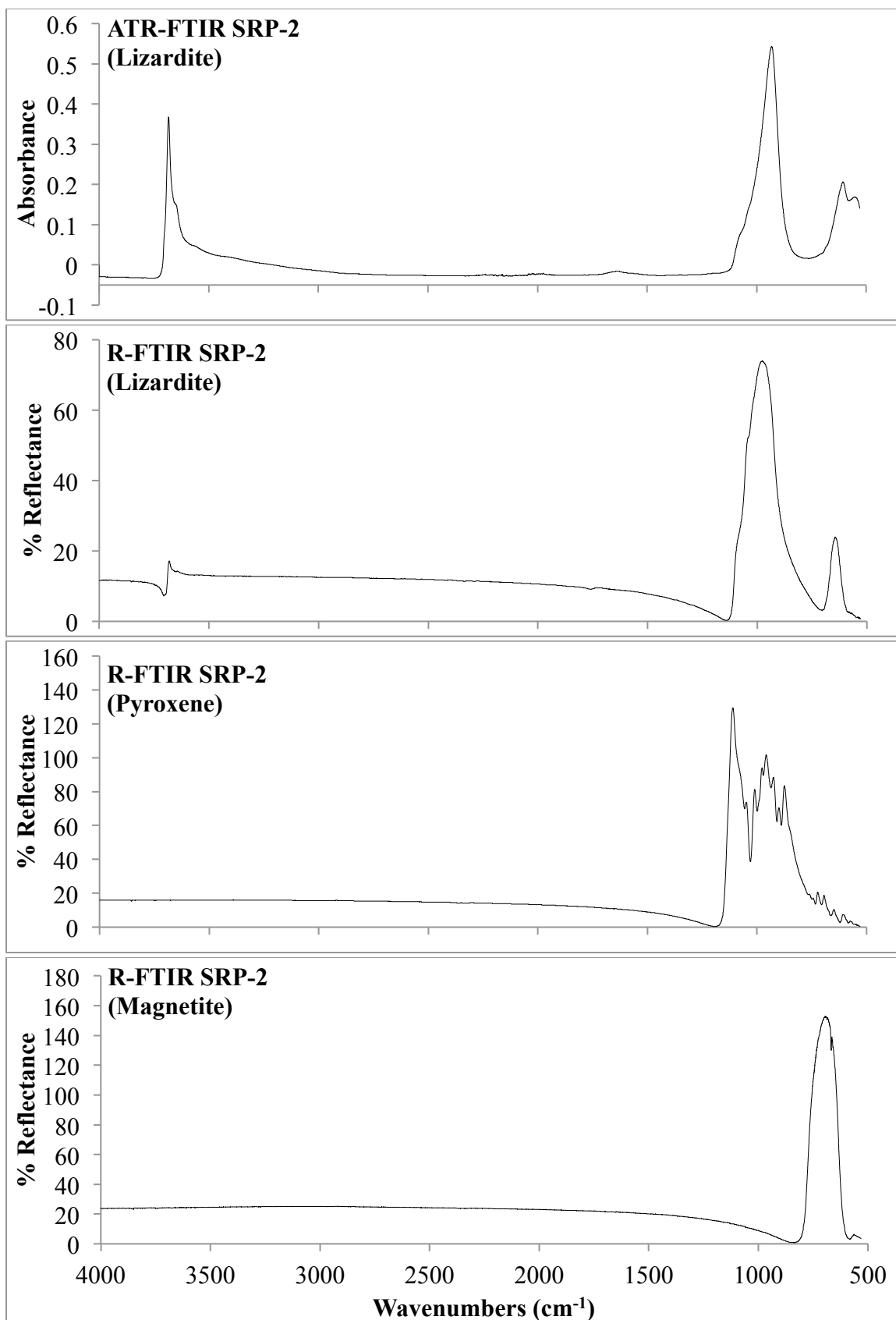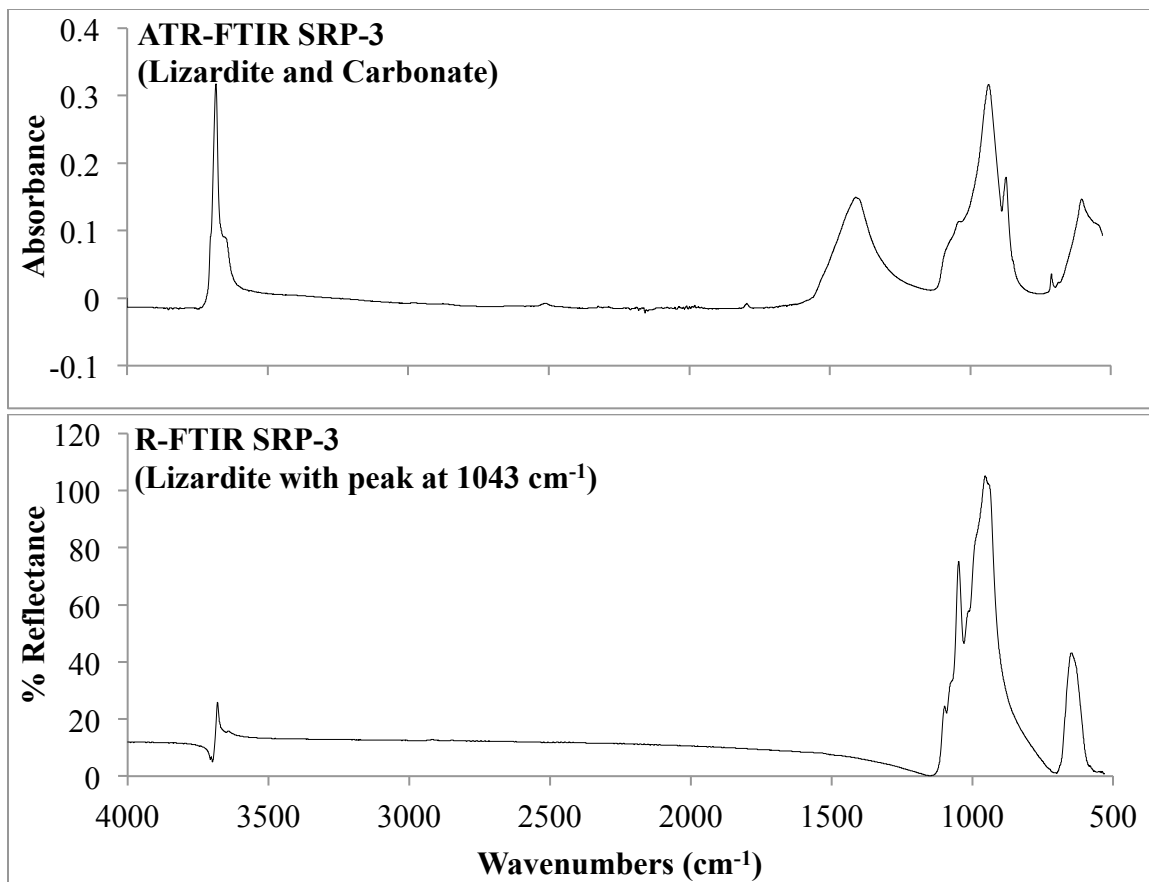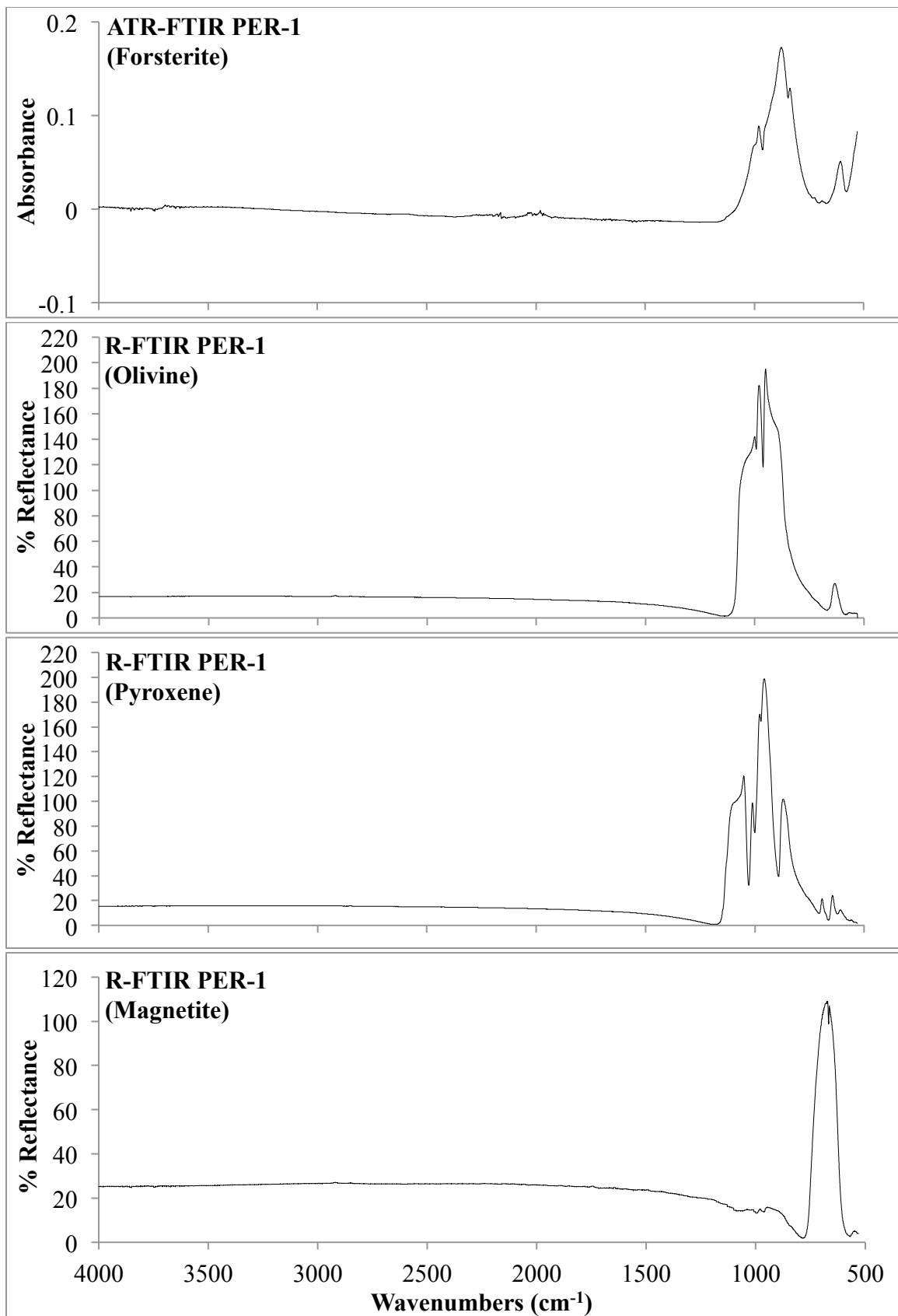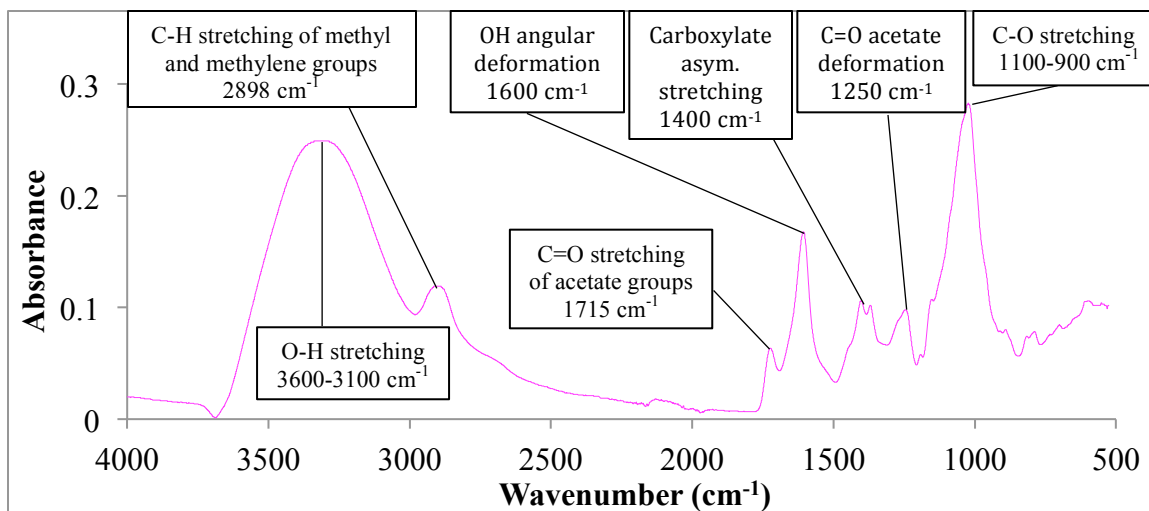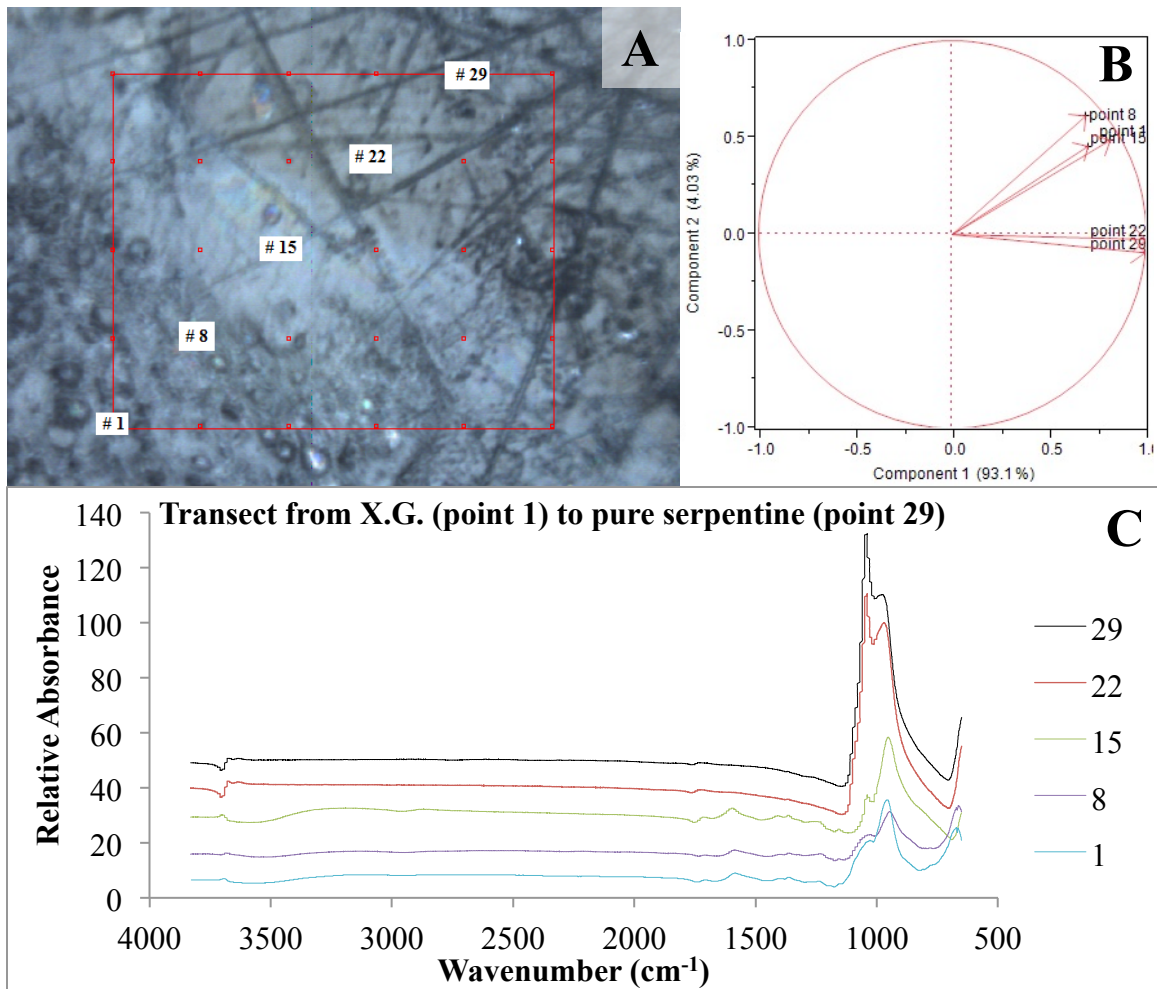
Figure 5

Figure 6

Figure 7

Figure 8

Figure 9

Figure 10

Figure 11

Figure 12

Figure 13

A

100 μm

Before cleaning surface with IPA

B

% Reflectance

40

20

0

After cleaning surface with IPA

C

% Reflectance

40

20

0

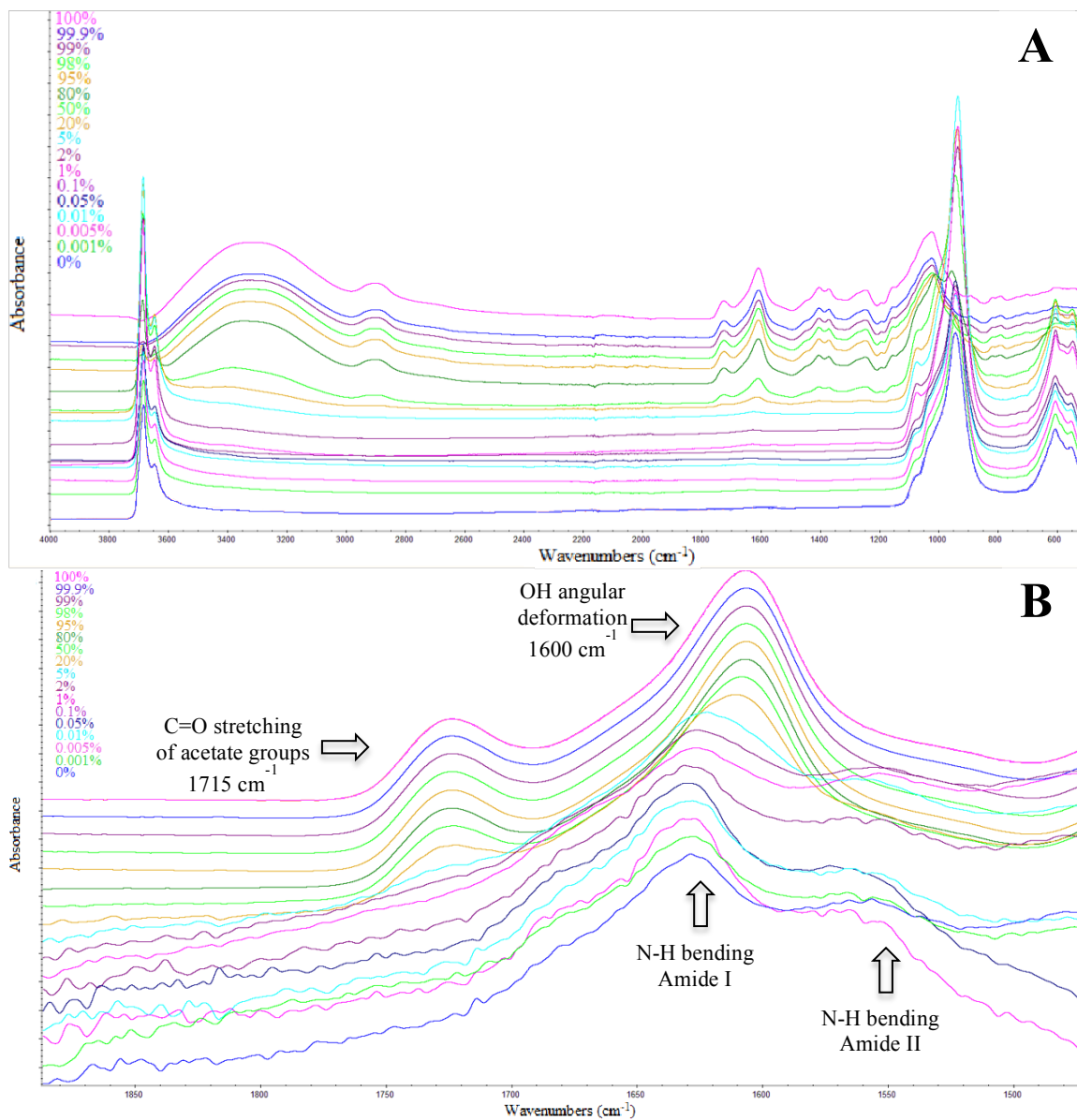4000 3500 3000 2500 2000 1500 1000 500

Wavenumbers (cm⁻¹)

Figure 14

Figure 15

Figure 16

Figure 17

Figure 18

Figure 19

Figure 20